The Dissertation Committee for Xin Xu

certifies that this is the approved version of the following dissertation:

Fabrication and Integration of Metasurfaces and Metagratings into Organic Photodetectors and Light Emitters

Commitee:

Ananth Dodabalapur, Supervisor

Andrea Alù

Seth R. Bank

Roger T. Bonnecaze

S.V. Sreenivasan

Fabrication and Integration of Metasurfaces and Metagratings into Organic Photodetectors and Light Emitters

by

Xin Xu

Dissertation

Presented to the Faculty of the Graduate School of

The University of Texas at Austin

in Partial Fulfillment

of the Requirements

for the Degree of

DOCTOR OF PHILOSOPHY

The University of Texas at Austin

August 2019

Fabrication and Integration of Metasurfaces and Metagratings into Organic Photodetectors and Light Emitters

by

Xin Xu, Ph.D.

The University of Texas at Austin, 2019

Supervisor: Ananth Dodabalapur

The field of optics has been transformed with the advent of high precision nanofabrication techniques that can be used fabricate subwavelength features in the optical regime. Advanced nanofabrication can be used to create engineered materials with optical properties unlike those found in nature and are impossible to achieve using conventional optics. Metasurfaces and metagratings are examples of these new types of engineered materials with unprecedented control over light. These metasurfaces and metagratings are composed of resonators at the nanoscale composed of either plasmonic or dielectric materials. The careful arrangement of these resonators can be used to create interfaces that can steer light in arbitrary directions, control the polarization and manipulate the phase. While there have been many studies into the fundamental design, fabrication, and characterization of these new engineered optical materials, there is relatively fewer work on integrating and implementing these materials into practical optical devices. This work will therefore be focused on the fabrication and integration of metasurfaces and metagratings into organic photodetectors and organic light emitters.

In the first part of this work, we integrate a metasurface into an organic photodetector. Ultrathin flexible light sensors have many interesting applications but have drawbacks in their efficiencies because the light absorbing material is too thin to absorb a large degree

of the incident light. For this application, the addition of a metasurface can be used to enhance the absorption and make the device appear optical thicker without adding too much additional thickness. We experimentally demonstrate metasurface-enhanced photoresponse in organic photodetectors. We have designed and integrated a metasurface with broadband functionality into an organic photodetector, with the goal of significantly increasing the absorption of light and generated photocurrent from 560 nm up to 690 nm. Our results show large gains in responsivity from 1.5X to 2X between 560 nm and 690 nm.

Secondly, we investigate the integration of metagratings into organic light emitting devices with the goal of enhancing emission. Organic light emitting diodes are a common device for mobile screens and televisions but suffer from to a relatively low external quantum efficiency due to generated light being trapped in waveguide modes in the high refractive index organic materials. We incorporated several different types of metagrating to enhance the output light coupling. These included gratings based on a square lattice, 1D periodic lines, and quasicrystal patterns. Discussed are the key parameters for the behavior of the enhancement, such as spacing of the grating from the backside reflector, the periodicity of the grating, and the type of grating. In addition, we study the angular emission pattern and how it differs with differing grating parameters, and also study the polarization dependence of the three patterns as well.

Contents

List of Figures

1 Introduction

Advances in nanofabrication has enabled the design and fabrication of new and interesting subwavelength optical structures that have generated a lot of interest in their ability to manipulate light in unprecedented ways. One class of these structures is the metasurface, an engineered interface composed of meta-atoms of subwavelength thickness that can be arranged to create the desired effect at the interface [1–3]. These meta-atoms are usually nanoresonators composed of either plasmonic or dielectric materials. Metasurfaces have been used to demonstrate control over many optical properties such as propagation direction, phase, and polarization.

Another more recently developed structure are metagratings [4–7]. Metagratings are periodically arranged arrays of either plasmonic or dielectric scattering particles above a reflecting backplane. By carefully controlling the arrangement of the scattering particles along with the spacing between the particles and the backplane, metagratings can have excellent control over impinging fields. The key advantage of metagratings over metasurfaces is that the spacing of the grating does not necessarily need to be subwavelength. This makes fabrication of these gratings slightly easier compared to their metasurface counterpart.

In this dissertation, both metasurfaces and metagratings are fabricated and integrated into optical devices. Generally optical devices will either need to absorb light or emit light as part of their operation. The works presented here will show how including a metasurface inside a photodetector can improve the absorption the therefore the performance of the a photodetector, and how a metagrating reflector can be used to control and enhance the emission profile of an organic light emitter with obvious applications to the world of organic light emitting devices (OLEDs).

1.1 Light Absorption Enhancement

Light sensing with photodetectors are an important part of modern electronics from cameras on mobile devices to fiber optic communication networks. Very often however, photodetector efficiencies and responsivities need to be enhanced over a range of wavelengths over which the absorbing material is not strongly absorbing because either the absorbing material has a weak natural absorption at those wavelengths, or more recently as we move towards ultra-thin or even 2D materials, there is simply not enough material to achieve strong absorption [8–12]. To counteract this, techniques to increase the absorption have been developed such as the incorporation of Fabry-Perot cavities, plasmonic structures, photonic crystal architectures, etc [13–17]. Examples, can be seen in Figure 1. However, there are disadvantages to each of these techniques such as only increasing light absorption in a narrow band, dependence on specific material resonances, and increased bulk and thickness of the overall device.

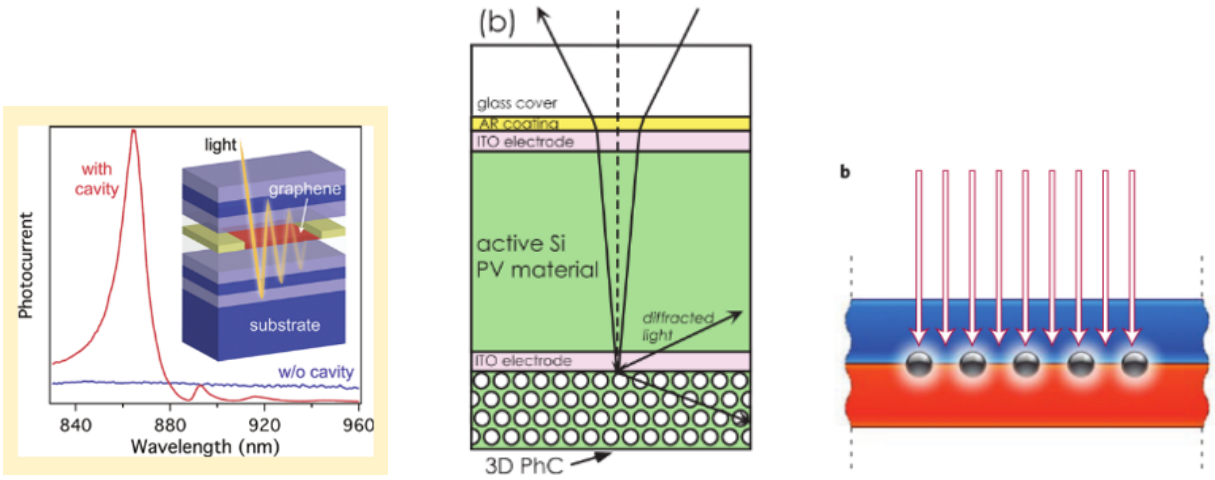

(a) Fabry-Perot (b) Photonic Crystal (c) Plasmonic Resonance

Figure 1: Three examples of light trapping schemes to increase light absorption in thin-film and 2D absorbers. (a) Fabry-Perot nanocavity to increase absorption in a graphene photodetector [13]. (b) Photonic crystal to increase absorption in a thin-film silicon solar cell [17]. (c) Light trapping via localized surface plasmons in metal nanoparticles in a thin film semiconductor [16].

Phase-gradient metasurfaces integrated into light absorbing devices is another option to increase the absorption of photodetectors. These metasurfaces control the direction of light

as light reflects off of the metasurface. Steering the light beam to extend the light travel path within a photodetector increases the sensitivity and efficiency of the photodetector. Phase-gradient metasurfaces overcomes many of the limitations of previous techniques. They work across a relatively broadband set of wavelengths; their response is more closely linked to the geometry of the surface design rather than the specific material resonances; and lastly, they are by definition thinner than the wavelengths they interact with, which minimizes the additional thickness that their inclusion in a photodetector adds [2, 3, 18–23]. Metasurface patterning can also greatly benefit from advance lithography techniques, such as nanoimprint lithography, which is a mechanical nanofabrication technique that reproduces a pattern from a master [24–26].

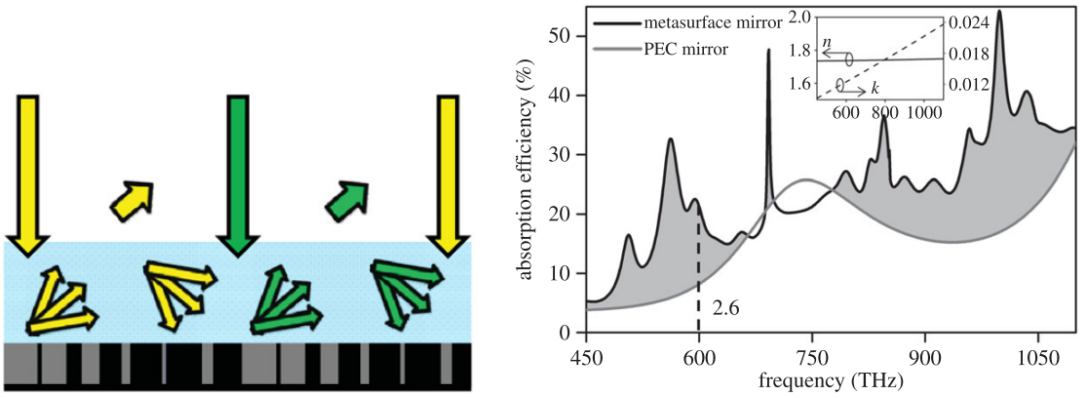

(a) (b)

Figure 2: (a) Using a metasurface for light trapping in an organic solar cell. The active layer is backed by a metasurface that imparts the desired linear momentum to the impinging wave. Arrows indicate the process of light trapping. (b) Absorption spectrum showing the increased absorption efficiency due to the presence of the metasurface [23]

The goal of this section of the dissertation is to fabricate phase-gradient metasurfaces and to design photodetectors that allow for the integration of metasurfaces. The fabrication and integration of a metasurface into a thin-film organic photodiode will be discussed. The metasurface extends the light propagation time within the organic absorbing layer, making it appear optically thicker which leads to increased absorption and larger photocurrents.

1.2 Light Emission Enhancement

Commercially available organic light emitting diodes (OLEDs) shows up in many typical consumer devices such as mobile phones and televisions. They offer many key advantages over their inorganic counterparts such as being thinner, lighter, and can be fabricated onto flexible substrates [27–29]. However, one key limiting factor is the outcoupling efficiency of the light due to the trapping of light inside the waveguide modes of the OLED as can be seen in Figure 3 [30, 31]. Unlike inorganic LEDs, OLEDs cannot be directly shaped and patterned to increase their outcoupling efficiency due to their more fragile nature.

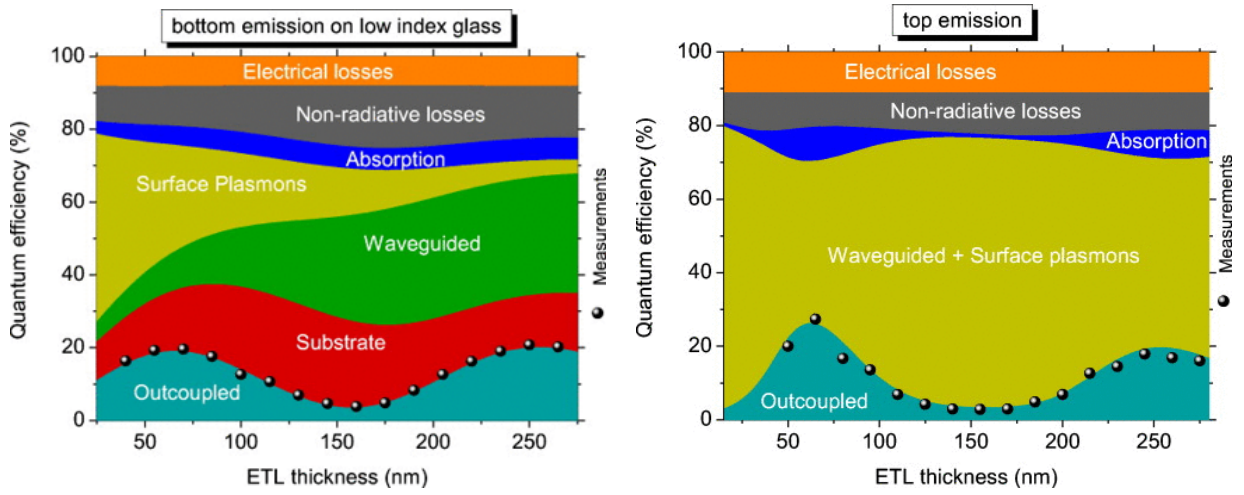

(a) (b)

Figure 3: Loss mechanisms inside a (a) bottom emitting OLED (b) top emitting OLED. As can be seen, a large amount of generated light is loss in waveguide modes due to the higher index of refraction of the organic layers compared to air leading to total interal refraction [30].

There have been several techniques developed to increase light emission such as shaping the transparent substrate, micro-lens arrays on the substrate, micro-cavities, photonic crystal outcouplers, etc [31–39]. However, many of these techniques are only applicable towards bottom emitting OLEDs and focus on engineering the transparent bottom substrate where the light is emitted. Top emitting OLEDs where the light comes out of the top of the structure rather than at the bottom substrate have much less applicable methods for light emission enhancement [28]. Many commercially available OLEDs are top emitting because

of their compatibility with active matrix transistor back planes [28].

The incorporation of a metagrating reflector can be applied to enhance light emission in top emitting OLEDs. The metagrating reflector is used to break the generated light out of waveguide modes present in the structure due to the higher index of refraction that the organic materials have compared to air (n = 1.7 for organic materials and n = 1 for air). The metagrating can also be used to tailor the emission by changing the geometry of the grating and the spacing between the grating layer and the metal back reflector. Also as before with metasurfaces, metagratings benefit from their ability to be patterned in the future by nanoimprint lithography [25, 26].

The goal of this section of the dissertation is to fabricate a variety of patterns of metagrating such as periodic lines, circular posts arranged in a square array, and lastly circular posts arranged in a quasicrystal. Then these patterns are incorporated into an organic light emitting device to study how they impact the emission pattern. These metagrating patterns break the waveguide modes inherent in the OLED structure and strongly enhances outcoupling of those modes into the air. The enhancement of the surface normal emission will be studied, as well as changes in the angular emission pattern. The reflectance of these metagratings will be measured and compared to a flat metal mirror. Lastly the polarization of the emitted light will be measured as well.

2 Metasurfaces and Metagratings

Broadly the field of metamaterial optics refers to the arrangement of subwavelength components to create optical effects that cannot be achieved in nature. These subwavelength components are composed of either dielectric or plasmonic materials and are frequently modeled as Mie-type resonators. In this work we will be talking about two types of metamaterial arrangements: the phase-gradient metasurface, and the metagrating metasurface. While there has been a lot of work on the design and theory of metasurfaces, less work has been done on the actual application of the theory into real-world devices. This dissertation will focus on primarily on the fabrication and integration of these metasurfaces into practical optical devices. This chapter will be a brief theoretical overview of these metasurfaces and how they are designed.

2.1 Phase-Gradient Metasurfaces

A metasurface is an artificial interface and is composed of an arrangement of subwavelength resonators that are placed in a specific way to achieve a desired optical effect. The thickness of hte metasurface has to be subwavelength as well, leading to to the "surface" aspect of the metasurface. Phase-gradient metasurfaces are a type of metasurface used to steer and manipulate light propogation by controlling the phase-front of light which is incident upon the metasurface. The starting point for phase-gradient metasurfaces starts with the generalized laws of refraction and reflection in Equation 2.1.1 and 2.1.2 respectively [19]. n_i refers to the index of refraction of the the initial material, n_t refers to the index of refraction of the second material past the interface where the transmission would occur. θ_i refers to the angle of the light with respect to the normal of the interface of the initial light path, θ_t refers to the angle of transmission, and θ_r refers to the reflection angle. Φ is the phase of the light, x is the axis of the interface, and λ_0 is the wavelength.

$$n_t \sin(\theta_t) - n_i \sin(\theta_i) = \frac{\lambda_0}{2\pi} \frac{d\Phi}{dx} \tag{2.1.1}$$

$$\sin(\theta_r) - \sin(\theta_i) = \frac{\lambda_0}{2\pi n_i} \frac{d\Phi}{dx} \tag{2.1.2}$$

Equations 2.1.1 and 2.1.2 reduce down to their more common variant when the term $\frac{d\Phi}{dx}$ is zero. This is the case for natural interfaces between two optical medias where there is no rapid change in phase at the interface. However with metasurfaces, the interface can be engineered and designed to create that phase-gradient leading to anomalous reflection and refraction.

One way of designing phase-gradient metasurfaces is to consider the surface impedance and admittance. Maxwell's equations lead to the interface conditions for electromagnetic fields that the tangential electric field $\mathbf{E}$ and the tangential magnetic field $\mathbf{H}$ must be continuous across the interface if there is no surface current present. However, we can engineer a surface that has an induced surface current when an incident electromagnetic field impinges upon it. This leads to the interface conditions as follows [40]:

$$\hat{n} \times (\mathbf{H}_2 - \mathbf{H}_1) = \mathbf{J}_s \tag{2.1.3}$$

$$\hat{n} \times (\mathbf{E}_2 - \mathbf{E}_1) = -\mathbf{M}_s \tag{2.1.4}$$

Here $\mathbf{E}_1$ and $\mathbf{E}_2$ refers to the electric field in material 1 and material 2 respectively which is split by an interface, $\mathbf{H}_1$ and $\mathbf{H}_2$ refers to the magnetic field in material 1 and 2 respectively, and $\mathbf{J}_s$ and $\mathbf{M}_s$ refers to the electric surface current and magnetic surface current respectively. The surface currents can then be expanded by their relationship with the surface admittance and impedance leading to the following equations [40]:

$$\hat{n} \times (\mathbf{H}_2 - \mathbf{H}_1) = \frac{1}{2}\bar{\bar{Y}}_e(\mathbf{E}_{2t} + \mathbf{E}_{1t}) \tag{2.1.5}$$

$$\hat{n} \times (\mathbf{E}_2 - \mathbf{E}_1) = -\frac{1}{2}\bar{\bar{Z}}_m(\mathbf{H}_{2t} + \mathbf{H}_{1t}) \tag{2.1.6}$$

Here $\bar{\bar{Y}}_e$ and $\bar{\bar{Z}}_m$ refers to the electric surface admittance and the magnetic surface impedance respectively while the subscript t refers to the tangential component of the fields. Generally since most materials are not magnetic, it is rather difficult to properly control the magnetic surface impedance, so we instead focus on the electric surface admittance. It turns out that one can control the surface admittance by designing the metasurface with a series of alternating plasmonic and dielectric materials. As can be seen in Figure 4, we can control the surface admittance by changing the ratio of the silver and a dielectric material with index $n = 3.46$.

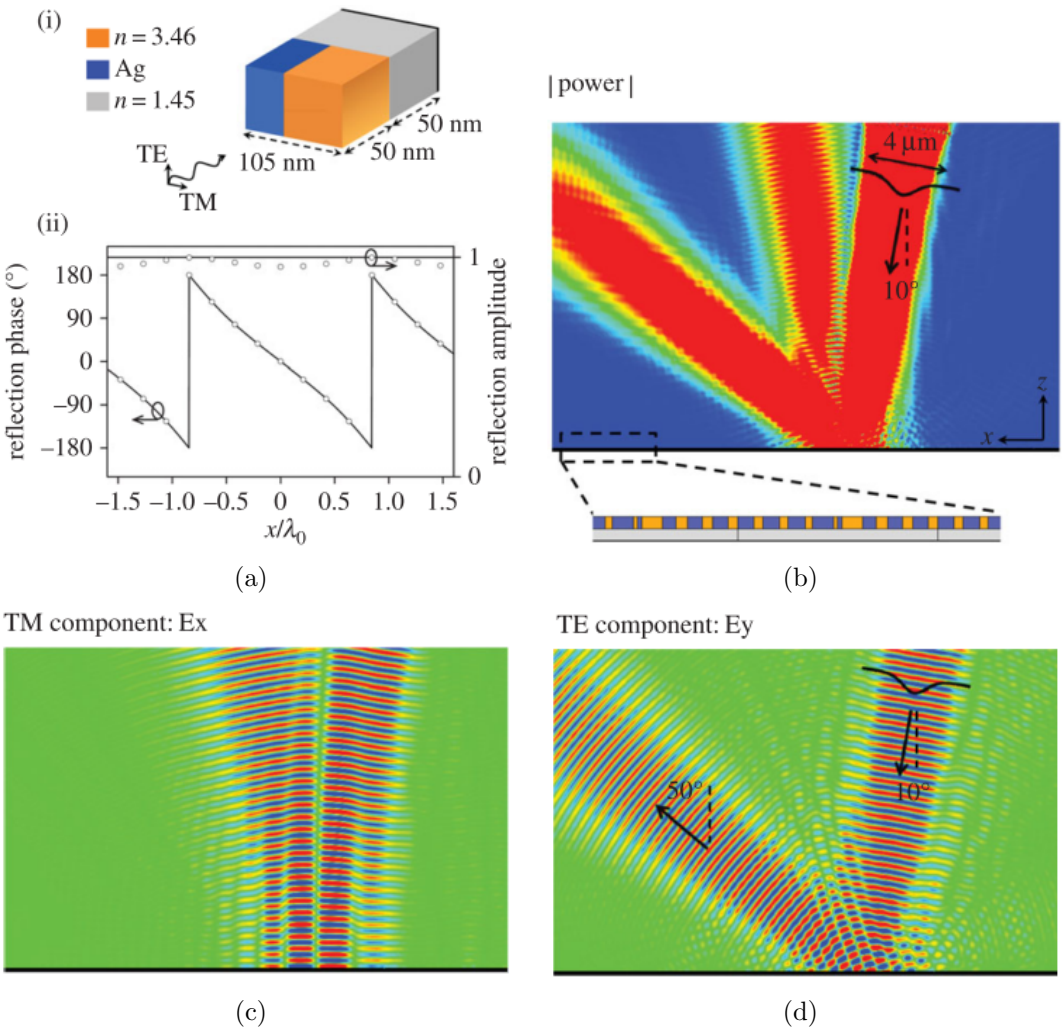

Figure 4: (a)(i) Surface admittance units are a blend of dielectric material and plasmonic material. The admittance of one unit can be controlled by the relative ratio of the two materials. (ii) Local reflection coefficient that will reflect the incident TE wave. (b) Power density when the metasurface is illuminated by circularly polarized light at 500 nm. (c) TM and (d) TE components of the electric field [23]

2.2 Metagratings

Metagrating metasurfaces are distinct from phase-gradient metasurfaces because metagratings cannot be described by their surface impedances or by any sort of localized reflection and transmission constant the way a phase-gradient metasurface can be [7]. Instead they are composed of diffraction gratings where the grating elements are plasmonic or dielectric nanoresonators. These resonators are suspended some distance above a metal reflecting

back plane with a dielectric material in between the grating elements and the reflecting backplane [4]. The periodic array creates a distinct series of diffraction modes as light impinges upon it. By varying the height the grating is suspended above the backplane, all modes other than the desired mode can be suppressed [4].

Metagratings unique advantage compared to phase-gradient metasurfaces is that while the nanoresonators inclusions are subwavelength, the arrangement of the resonators need not be deeply subwavelength the way that phase-gradient metasurfaces geometry requires. An example of the a metagrating can be seen in Figure 5.

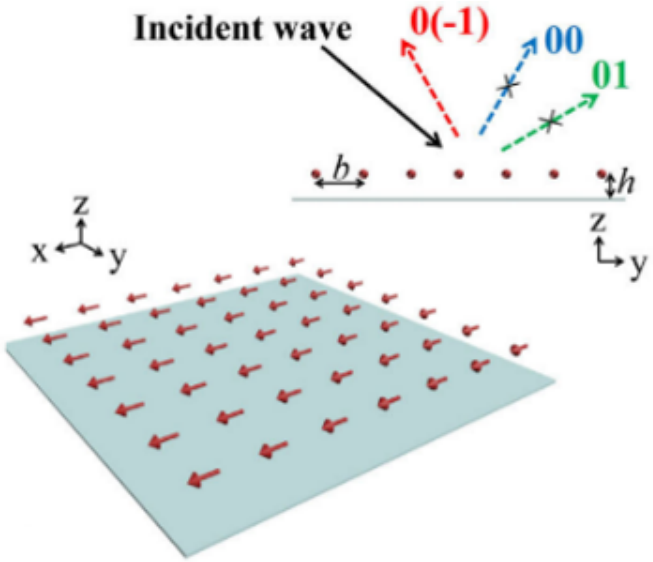

Figure 5: An example of a metagrating which is composed of an array of horizontal magnetically polarizable particles located over a ground plane. In this example, an incident wave impinges upon the metagrating and the reflection is in the 0(-1) Floquet mode while the other diffraction modes are suppressed. Key to the behavior of the metagrating is the spacing of the periodic inclusions labeled b and the height above the reflecting backplane labeled h.

For our application for inclusion inside an organic light emitting device, the metagrating design is rather complicated. The light emission from organics is best modeled as a series of randomly oriented dipole emitters [32, 41]. General design of metagratings usually assume the incident light is a plane wave at a specified angle which greatly simplifies the design problem [4, 5] . So instead of using a full analytical model to design the grating, we built

metagratings with three different types of grating patterns: a 1D line and space grating, a 2D square array of cylinder, and lastly a 2D quasicrystal array of cylinders. We then varied the key parameters of the metagrating such as the spacing between grating elements and the distance between the grating and the ground plane to observe the impact on performance.

3 Metasurface Enhanced Organic Photodetector [1]

In this study, a metasurface is designed and fabricated with a 1D periodic gold array patterned on top of SiO2 and surrounded by deposited zinc oxide (ZnO). A 3D mock-up of two repeating periods of the metasurface is shown in Figure 6, and the inset shows a scanning electron microscope image of four periods in the fabricated sample. This metasurface is

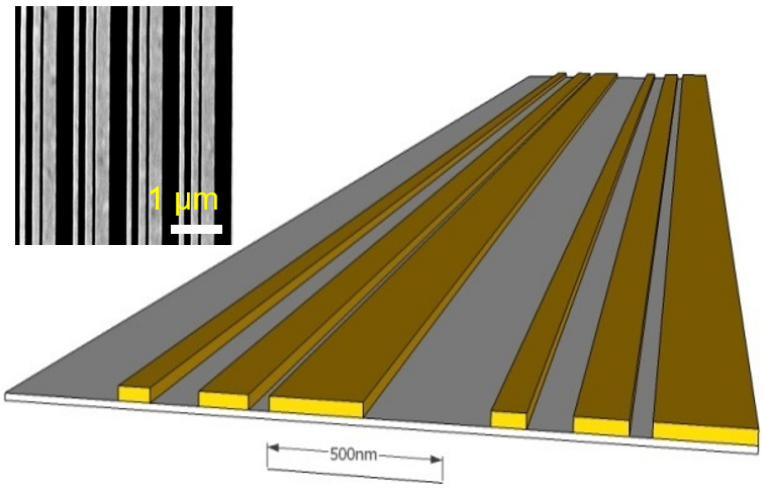

Figure 6: 3D mock-up of two periods of the metasurface. Inset: Scanning Electron Microscope image of finished metasurface, Scale bar is 1 micron

integrated into an organic photodiode structure to enhance the absorption and generation of photocurrent in a wavelength region where the organic absorbing material weakly absorbs. By adding a metasurface to the photodetector, we can increase the sensitivity of the photodetector across a relatively broadband spectrum by extending the light paths inside the photodetector.

[1] Based on previously published work [42]. Author contribution breaks down as follows: X.X. is responsible for the fabrication of the metasurface and the photodiode and all the electrical measurements and preparation of the paper. H.K. and N.M.E. designed and simulated the metasurface. H.K. also worked to prepare the paper. B.G. is responsible for the measurements with the spectrophotometer. S.V.S. guided the spectrophotometer work. A.A. is responsible for the overview of the design and simulation work. A.D. coordinated the overall research and designed and provided guidance for the experimental work. All authors contributed to the editing of the manuscript.

3.1 Design and Modeling of the Metasurface

The theoretical basis of the metasurface in this section of the dissertation starts from the concept of generalized Snell's law of refraction and generalized reflection. Recent studies show that metasurfaces designed based on generalized Snell's law can be used to control the light propagation direction [2, 3, 18–23]. The metasurfaces are used to control the direction of light reflected from the metasurface. The beam steering of the metasurface works best at the design wavelength, but provides high performance over a relatively wide range of wavelengths [43]. This inherent advantage of the metasurface approach over more conventional resonant light trapping solutions provides the freedom to target wavelengths where the light absorbing material is weakly absorbing, while still enhancing absorption in the surrounding wavelengths.

Diffraction channels can be opened into a specific direction by ensuring that the metasurface period D is equal to $\lambda/|sin(\theta_r)|$, where θ_r is the desired angle of reflection and λ is the design wavelength. When the surface admittance distribution is properly designed and implemented, light can be coupled into the desired diffraction order, which, if chosen to be far from the normal, and below the critical angle at the interface between the device and free-space, may lead to largely increased propagation paths, enhancing absorption. The admittance profile to optimize light trapping over a moderately broad range of wavelengths is derived from previous works by applying the optical properties of the constituent layers of the device [2, 3, 18–23]. After analyzing the ideal admittance profile for the desired propagation direction, the dimensions for the fabrication of the metasurface are defined and implemented.

The metasurface within the organic photodetector is designed to have 20 degrees reflection relative to normal incidence for a wavelength of 700 nm in free space. The period D is discretized into 4 unit cells, dragging the phase of incident light from 0 to 1.5π in steps of 0.5π. Figure 7 (a) shows a sketch of the metasurface integrated within the photodetector,

and Figure 7 (b) shows the case of a regular photodetector without metasurface. Alternating gold and ZnO are the materials used for the implementation of the metasurface.

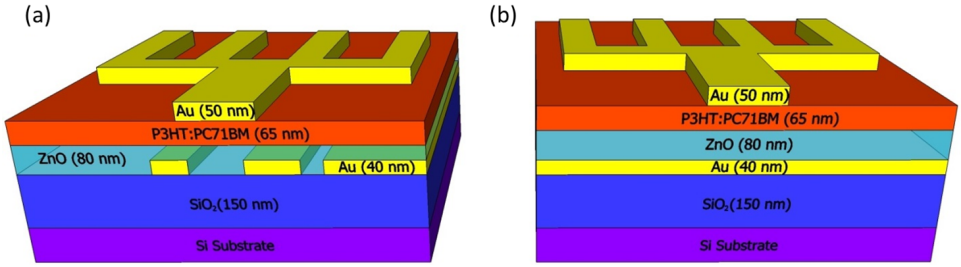

Figure 7: Schematic layer structure of the photodetectors. The top gold metal contact shape is not to scale. (a) Photodetector structure with metasurface which is designed to created a reflection deflection angle of 20 degrees. (b) Photodetector without the metasurface

After designing the metasurface shown in Figure 6 and integrating it into an OPD as shown in Figure 7, we ran a simulation with COMSOL Multiphysics to confirm how the metasurface tailors light propagation. With normal incidence at the design wavelength, energy efficiently couples to the desired diffraction order with up to 75 percent efficiency, demonstrating that the metasurface is highly effective at tailoring the light path and enhancing light trapping in the superstrate layer.

Simulations of the scattered E-field are shown in Figure 8. Comparing the field profiles between the metasurface integrated structure in Figure 8(a) and the scenario without metasurface in Figure 8(c), we can clearly see that the E-field is bent to the left (at 20 degrees), which increases the propagation path inside the photodetector, resulting in larger absorption. The metasurface works best at the wavelength of design, but it still provides good light trapping over a relatively broad wavelength range. While there is an expected natural dispersion with fixed periodicity, there is still an enhancement phenomenon away from the design wavelength, as predicted in [22] and seen in Figure 8(b).

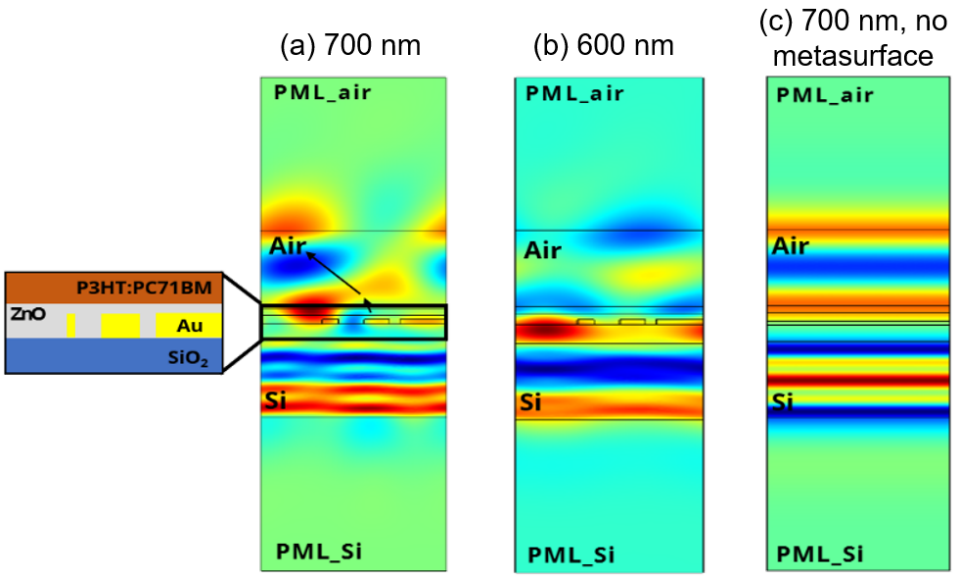

Figure 8: Simulated scattered E field in the z direction. The top metal contact is not simulated. (a) Simulation of the metasurface integrated photodetector at the design wavelength of 700 nm. The wavefront is tilted into the desired angle with high efficiency. (b) Simulation of the metasurface integrated photodetector at 600 nm. From this simulation, a metasurface response at wavelengths besides the design wavelength can be observed. (c) Simulation of a photodetector without a metasurface at 700 nm. The planar wavefronts of the normal reflectance can be observed.

3.2 Fabrication of Metasurface and Incorporation into Photodiode

In order to make a straightforward comparison between photodiodes with and without the inclusion of the metasurface, the substrate was patterned so that the two types of photodiodes would be fabricated side by side. Our design uses the gold metasurface as the bottom contact of the photodiode, and its performance is compared to the one with a flat and continuous gold bottom contact. Other than this modification, the two devices are identical and are fabricated on the same substrate. The metasurface was fabricated using e-beam lithography and metal deposition and lift off. On a substrate of silicon with 150 nm thick thermally grown silicon oxide, ZEP 520A was spun and patterned using a JEOL 6000 FSE E-beam. The pattern was developed using a bath of amyl acetate for 12 seconds. A layer of gold with a titanium adhesion layer was deposited with a Lesker Thermal Evaporator, and lift-off was performed in a Remover PG bath at 80 degrees C for four hours. The e-beam and lift-off

process can be seen in Figure 9.

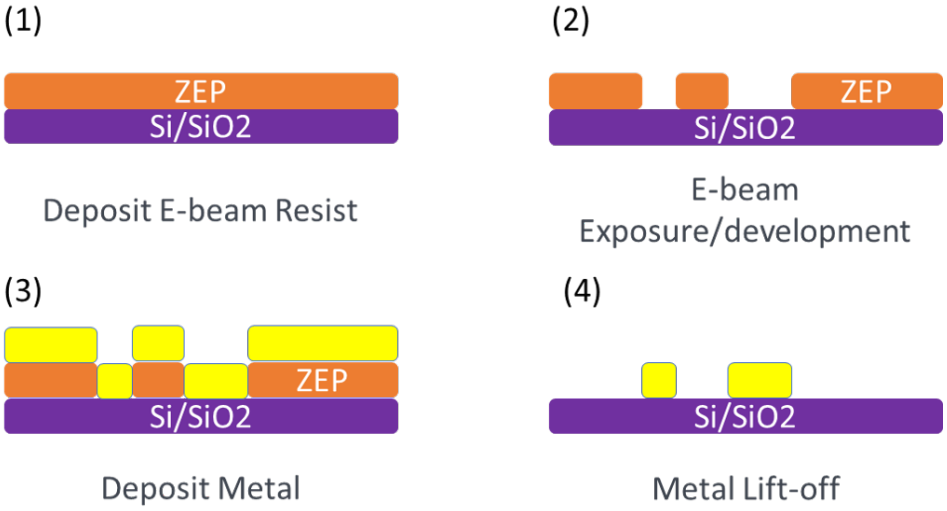

Figure 9: Fabrication of the metasurface with electron beam lithography.

Incorporation of a metasurface into an organic photodiode requires a modification of the standard organic photodiode structure. The standard organic photodiode is bottom illuminated, and is built on top of a transparent conducting substrate, such as ITO coated glass [44, 45]. However, this standard design does not work with our metasurface which is designed to change the reflection angle of incident light. In the conventional organic photodiode stack, the metasurface would have to be fabricated after the deposition of the organic layer, but the fabrication process of the metasurface would destroy the organic absorption layer. In our modified photodiode structure, as seen in Figure 7, the metasurface is fabricated on a substrate of thermally grown silicon oxide (SiO2) on a silicon wafer. Deposited above and around the metasurface is an electron transport layer of ZnO, which was spin-coated from a precursor of diethylzinc and annealed at 150 degrees C [46]. This method for depositing ZnO uses a low annealing temperature which protects the metasurface from possible damage by the gold deforming under high heat. The organic active layer is the polymer-fullerene blend of poly(3-hexylthiophene):[6,6]-phenyl C71 butyric acid methyl ester (P3HT:PC71BM), which was spin-coated from a precursor of the blend dissolved in dichlorobenzene [44]. This organic blend was selected because it is well studied and understood, and absorbs strongly in the

green but absorbs less at longer wavelengths, where the metasurface enhancement would be most obvious [9, 47–51]. The thickness and optical properties of the thermal SiO2, ZnO, and the organic blended film were measured using a Woollam Ellipsometer M-2000D. Lastly, finger shaped gold top contacts were deposited by thermal evaporation through shadow masks which are patterned to leave gaps for light to pass through as can be seen in Figure 10.

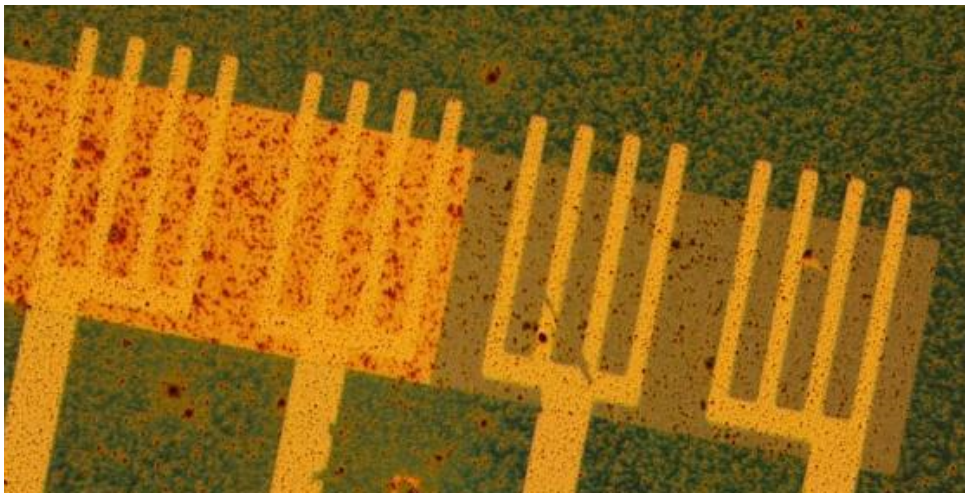

Figure 10: Top down view of four completed organic photodiodes . The two devices on the left are on unpatterned gold, while the two on the right are on the metasurface. The top metal contact finger design leaves enough space for light to pass into the devices.

3.3 Results and Analysis

The photodiodes were measured in a vacuum environment to prevent degradation of the organic film. The current of each photodiode was measured while sweeping the voltage from 1 V to -1 V, under light and under dark conditions. A xenon lamp white light source with narrow band-pass filters (FWHM = 10 nm) was used as the light source with filters from 710 nm down to 600 nm in 10 nm increments and then down 560 nm in 20 nm increments. The intensity of light with each individual filter was measured using a ThorLabs PM100D Power Meter with a silicon photodiode with sensitivity from 400 nm to 1100 nm. The measured light intensity was then used to calculate the responsivity [52].

Photodiodes with metasurface back contact show a large increase in reverse bias photocurrent

compared to the photodiodes with unpatterned metal contact. This trend held across multiple devices and samples. Figure 11 shows the photocurrent and responsivity of photodiodes with and without the metasurface. It can be seen that there is an increase in responsivity of 2X from 560 nm up to 660 nm at which point the performance increase gradually drops down to 1. Also, it is important to note that across this entire range from 560 nm to 710 nm there is no loss in performance when comparing metasurface devices to devices without metasurfaces.

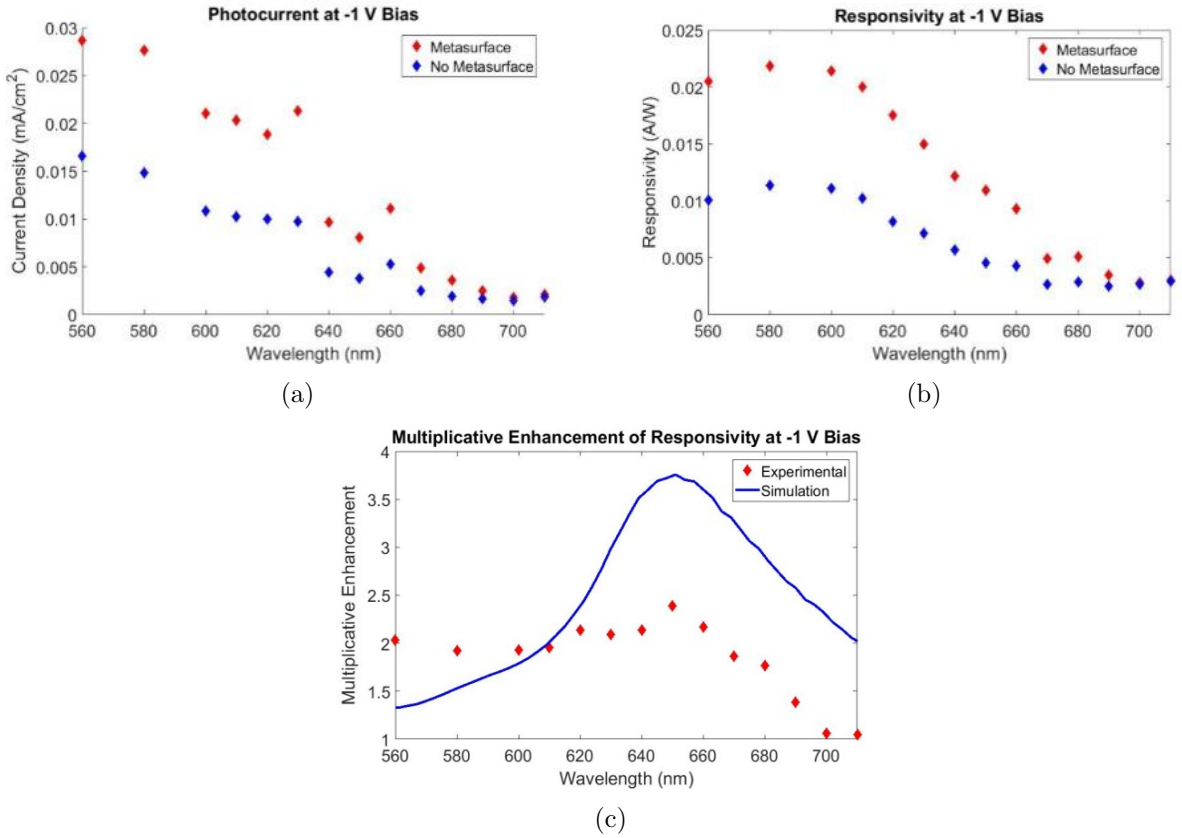

Figure 11: Results from experimental organic photodiodes. (a) Photocurrent of photodiodes with and without metasurfaces. (b) Responsivity of photodiodes with and without metasurfaces. (c) The multiplicative enhancement of responsivity of photodiodes with metasurfaces compared to photodiodes without metasurfaces for experimental devices and simulated devices.

The general trend of the experimental results match those in simulations, however the extent of increase in the measured photocurrent in metasurface containing devices is slightly less than that predicted numerically. This can be attributed to several factors. First, the

fabrication of the metasurface will not result in perfectly rectangular gold lines. Second, mismatches in film thickness are expected to impact the performance. Lastly, the simulation makes the assumption of perfectly smooth flat interfaces, but actual fabricated devices have rough interfaces as the films conform to the patterned metasurface. Interestingly enough, from 560 nm to 610 nm the experimental results actually outperform the theoretical predictions. This is due to the simulation predicting an internal electromagnetic resonant effect due to the arrangement of all constituent layers of the photodiode. However, the experimental devices are never perfectly flat or smooth, leading to a weakening of the resonance that lowers the actual measured photocurrent, thus improving the comparison between metasurface and non-metasurface device.

In order to validate the enhancement of photocurrent, and confirm that it is indeed due to increased light absorption, samples without top contacts were exposed to light of varying wavelengths and imaged with a spectral camera. The imaged reflectance of an aluminum mirror was taken as a baseline to calculate the reflectance of photodiodes. Figure 12 shows the reflectance of the metasurface area compared to the reflectance of the unpatterned metal area at various wavelengths from 560 nm up to 700 nm. The clearly darker metasurface region means that there is less reflectance compared to the unpatterned metal area, and we can safely deduce that the metasurface area is indeed absorbing more strongly than the area with no metasurface.

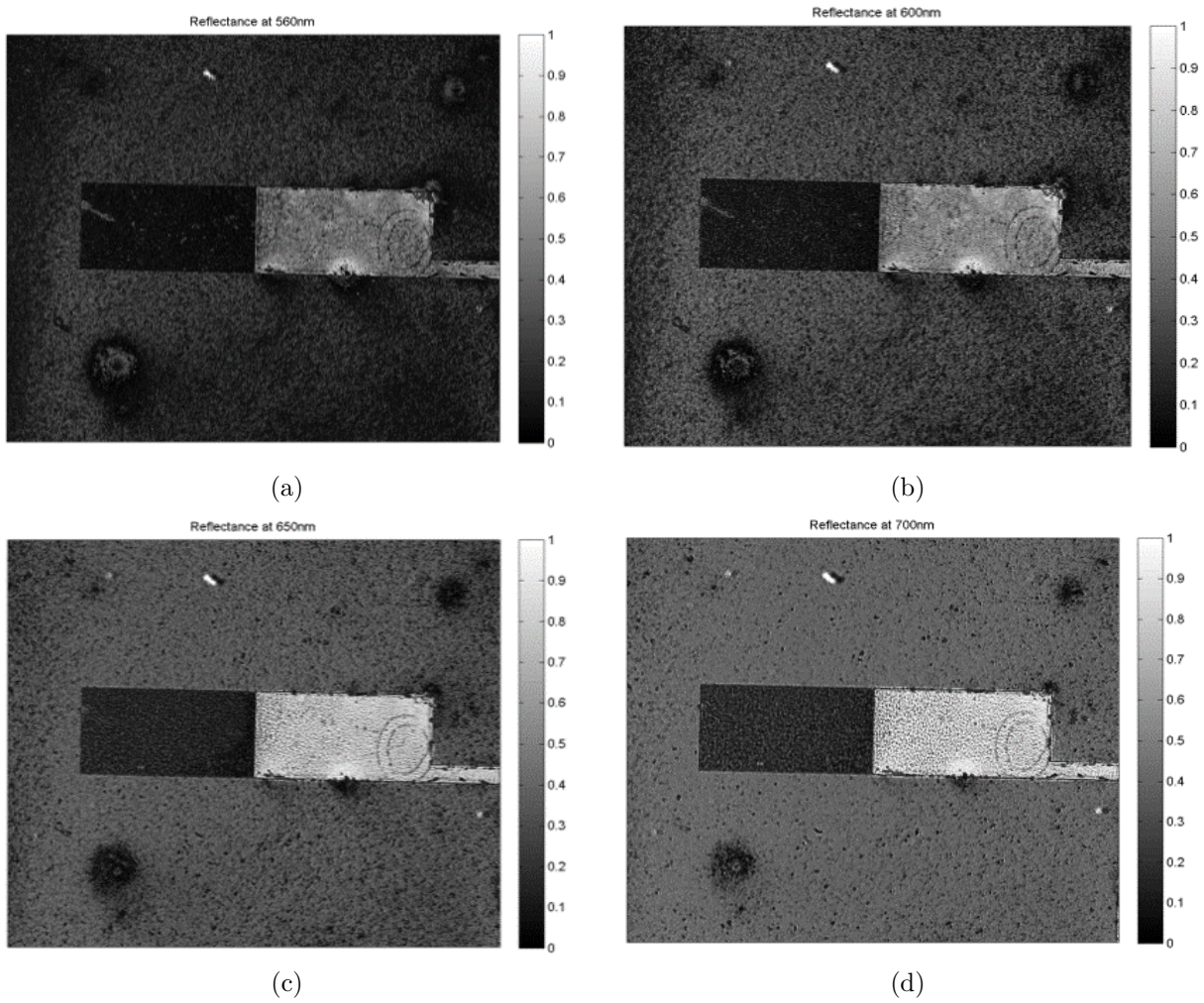

(a) (b)

(c) (d)

Figure 12: Measured reflectance at varying frequencies of light of the photodiode stack with an aluminum mirror used as a reference reflection of 1. The left area is the metasurface, while the right area is unpatterned gold. (a) 560 nm, (b) 600 nm, (c) 650 nm, (d) 700 nm. The clearly darker metasurface regions show lower reflectance which means increased absorption.

3.4 Discussion and Conclusion

We have demonstrated the benefit of the integration of a metasurface to increase organic photodiode performance from 560 nm to 690 nm. There are several key advantages of this technique. One is its inherent flexibility: the metasurface geometry can be designed to increase absorption of a wide range of weakly absorbing thin films over a broad range of wavelengths. Another advantage is the potential of the metasurface with improved lithog-

raphy and metal patterning. By making finer metal patterns we can increase the degree to which we bend light to go beyond 20 degrees, which would lead to a further enhancement in performance. This is particularly beneficial to weakly absorbing materials, such as graphene. We stress that this technique is not limited to making photodetectors. There are many parallels between photodetectors and solar cells, and metasurfaces would be appropriate to increase the absorption in thin film solar cells, particularly over wavelengths where absorption is weak [53].

In summary, we demonstrated the experimental realization of metasurface-enhanced organic photodetectors with significantly increased absorption of light and generated photocurrent over a large range of wavelengths, from 560 nm to 690 nm. We described how the metasurface can be integrated with the fabrication of an organic photodiode. Our results show large gains in responsivity from 1.5X to 2X between 560 nm and 690 nm. This general approach of using metasurfaces is very promising for a number of photodetector and photoabsorbing materials with low absorption.

4 Design and Fabrication of Metagratings

In this chapter, we will discuss the design and fabrication of metagratings for their eventual integration into an organic light emitting device. Organic light emitting diodes (OLEDs) suffer from low external quantum efficiency with one large loss mechanism being that the generated light is coupled into waveguide modes that do not leave the OLED [30]. The goal of including a metagrating is to redirect the light that would normally be totally internally reflected into modes that propogate out of the device.

The redirection of light for OLEDs is complicated because the light generated by organic materials is best modeled as a series of randomly oriented dipole emitters [32, 41]. This means that in comparison to the problem of light input coupling for photodetectors, where we assumed the light is a normally incident plane wave, the redirection of randomly oriented generated light is much trickier. It is for this reason, that there is not an analytical solution to determine the "best" performing metagrating for OLEDs. Instead we patterned several types and studied their behavior and performance.

Three different types of metagratings were designed and fabricated for this work: a 1D periodic line and space pattern, a 2D square array of cylinders, and lastly a 2D array of cylinders arranged in a quasicrystal pattern. The first two patterns are faily common and easily designed, but the last pattern, the quasicrystal, is rather unique and its design and fabrication will be talked about in depth in this chapter.

4.1 Low Temperature Sol-Gel Oxides

Metagratings are by definition a series of periodic resonators at a specific distance above a reflecting backplane. In our implementation of the metagrating, the spacing between the reflecting backplane and the perodic inclusions will be filled by a dielectric material,

specifically amorphous zirconium oxide (ZrO_2). We created a dielectric film that can be generated from a sol-gel process with a low temperature anneal for this metagrating work. The sol-gel process allows us to bypass costly and throughput limited deposition techniques such as sputtering dielectrics in high-vacuum chambers. The low temperature anneal is required to limit any sort of damage to the reflecting backplane and has the added benefit of increasing compatibility with a wider range of fabrication flows protecting potentially delicate components already existing on a substrate on which an OLED might be fabricated on. The development of this low temperature process required us to modify an existing sol-gel process for ZrO_2 which used a high temperature anneal as seen in Figure 13.

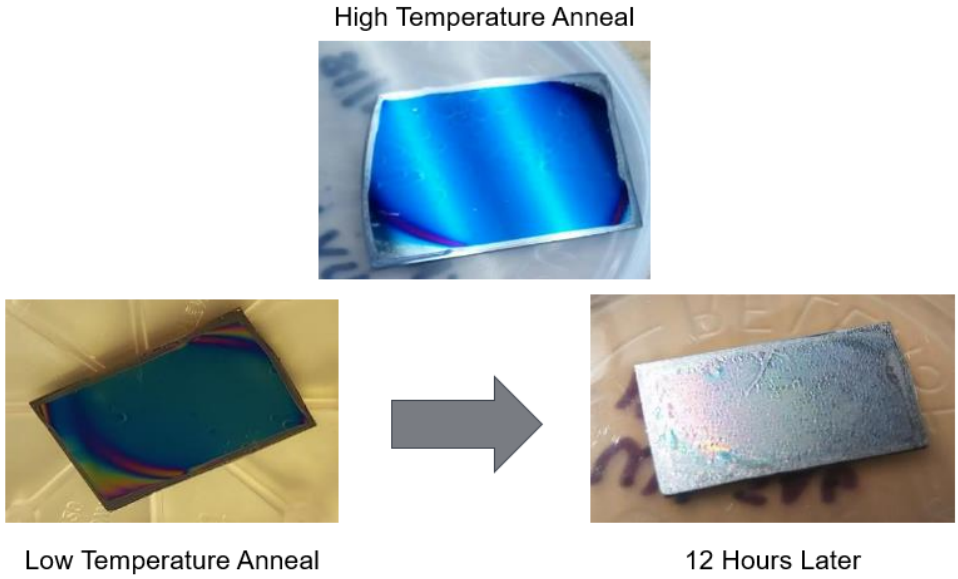

Figure 13: (Top) Sol-gel process spin coated ZrO_2 that is annealed at 500°C. (Left) Sol gel process spin coated ZrO_2 that is annealed at 120°C (Right) Same low temperature annealed film after 12 hours. Without the high temperature anneal, the film did not oxidize properly and is not air stable.

Sol-gel process have already been developed for many metal oxides, but they usually have a high temperature anneal as part of the oxidation process [54]. Previous work with this ZrO_2 sol-gel recipe called for an anneal at 500°C. However, we have found that we can encourage oxidation of the sol-gel precursor film into an oxide by exposing the samples to UV while under a low temperature anneal [55]. The UV light breaks down diatomic oxygen molecules into single atom oxygen which then oxidizes with the sol-gel precursor film to form

the desired metal oxide film. We used the PSD-UVT from NovaScan which is a benchtop tempeature controlled UV surface decontamination system for our low temperature anneal with UV exposure.

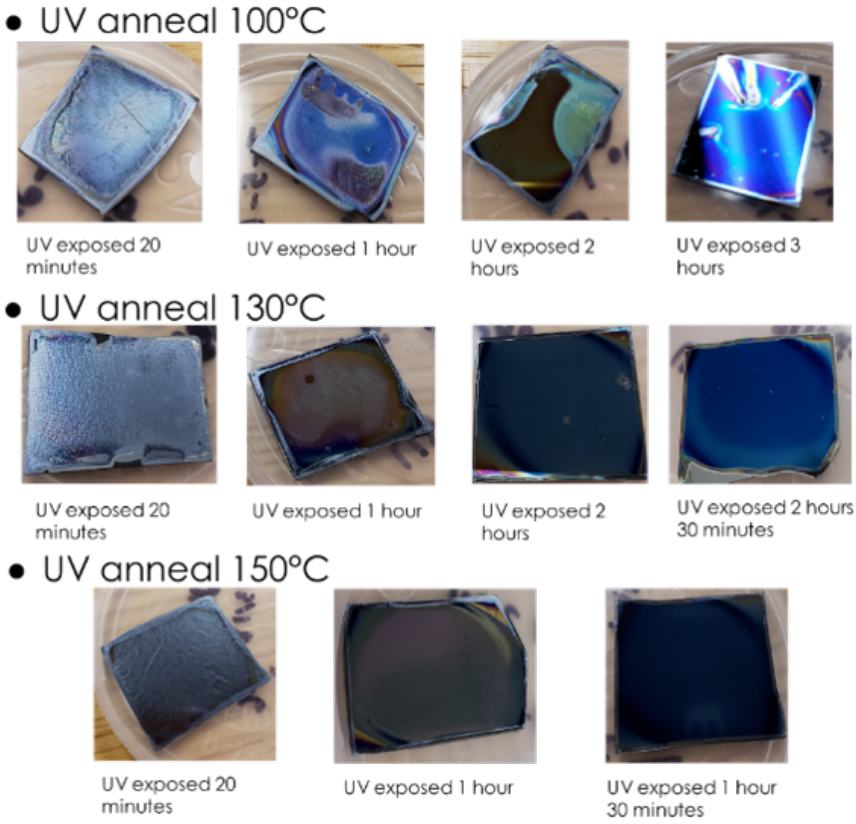

Figure 14: There is a clear relationship between higher temperature anneal and UV exposure time. The higher the temperature, the shorter the UV exposure time has to be to achieve proper oxidation of the ZrO_2 film. Without proper oxidation, the film degrades after exposure to ambient conditions.

The recipe for ZrO_2 sol-gel used in this work is zirconium chloride ($ZrCl_4$) and zirconium(IV) isopropoxide isopropanol complex (Zr-isopropoxide) dissolved into 2-methoxyethanol [54]. Solutions of this precursor are spin-coated onto prepared substrates. The spin-coating is done inside a nitrogen environment and this is followed by a 10 min anneal at 100°C inside the nitrogen environment. Afterwards, the samples are taken into ambient conditions and placed into the PSD-UVT where the sample is annealed and exposed to UV light at the same time. The UV exposure time necessary to create a stable film inversely correlates to the annealing temperature. A higher annealing temperature requires less UV exposure time

than a lower annealing temperature as can be seen in Figure 14.

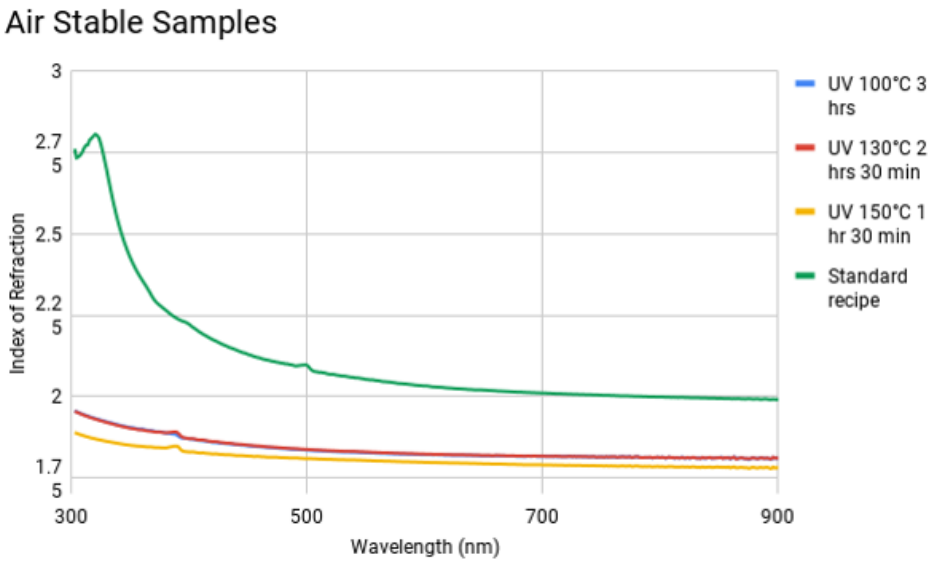

Figure 15: Index of refraction results for the air stable ZrO_2 oxide films on top of silicon substrates for different annealing conditions. Compared to the standard recipe with 500°C anneal, the modified UV anneal samples are much lower in index.

The resulting films were measured with a Woollam Ellipsometer M-2000D to determine their optical properties and it was found that compared to the high temperature anneal at 500°C, the UV annealed samples had lower indexes of refraction but the overall wavelength dependence was the same as can be seen in Figure 15. This, along with the fact that the samples that were UV annealed were thicker compared to the high temperature anneal, 123 nm thick for UV vs 65 nm for high temperature anneal, suggests that the UV annealed samples were more porous and included mixture with air. To test this hypothesis, an UV annealed sample of ZrO_2 was placed onto the 500°C hot plate for one hour and the thickness and index of refraction was remeasured. The results show that after the high temperature anneal, the sample had indeed become thinner (81 nm) while at the same time the index of refraction did increase as seen in Figure 16.

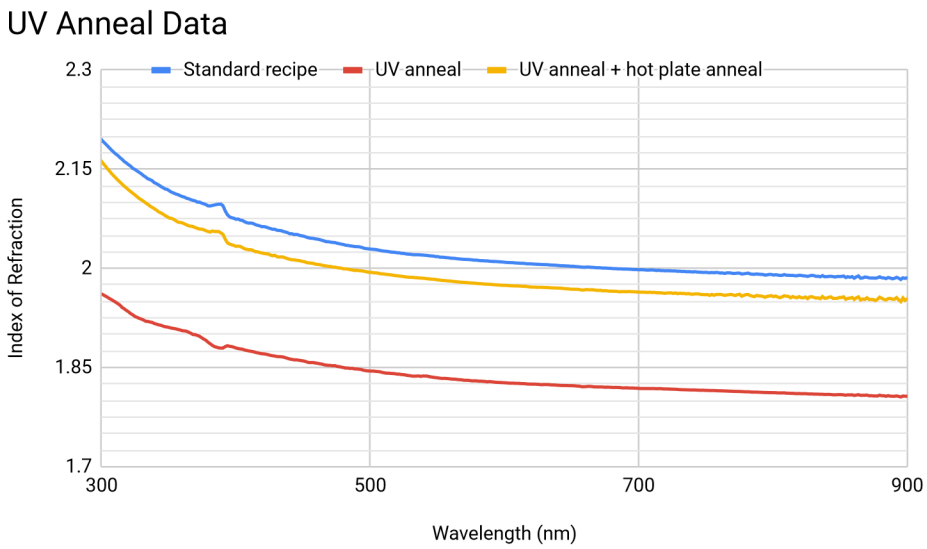

Figure 16: UV annealed ZrO_2 has a lower index of refraction (red line) compared to high temperature annealed oxide samples (blue line). However, when a UV annealed ZrO_2 sample is then also annealed at high temperature the resulting film has an index of refraction closer to that of the films that were only annealed at high temperature.

4.2 Designing the Quasicrystal Pattern

One concern with periodic metagratings is the polarization of the emitted light. OLEDs for commercial applications such as televisions and mobile displays use unpolarized light. A metagrating with a grating pattern based on a quasicrystal offers a potential solution to that problem. Quasicrystals are structures that are highly ordered but have no periodicity [56]. They have large amounts of rotational symmetry but no translational symmetry. It is these exact two properties of quasicrystals: highly ordered, no periodicity, which leads them to be an interesting candidate for metagratings. The highly ordered property means that the shape and design of the quasicrystal can be controlled and manipulated in a way that a random pattern could not be, and the lack of periodicity and high rotational symmetry means that the chance of a polarization dependent response is minimized.

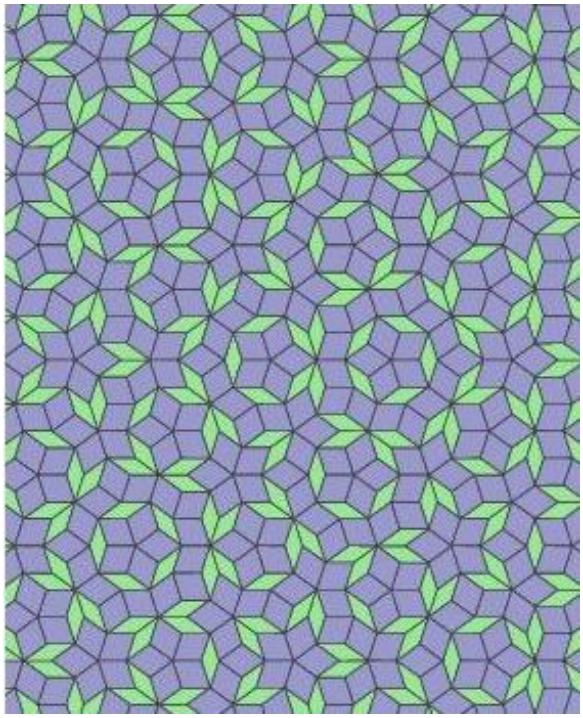

Figure 17: Penrose Tiling Type Three (P3). This forms the basis of our quasicrystal pattern [57]

A large area quasicrystal pattern was generated to form our metagrating. The pattern chosen is called a Penrose tiling type three or P3 tiling [58] which is composed of two rhombuses of equal sides but different angles and can be seen in Figure 17. These two rhombuses can then be broken down into a set of four distinct triangles. This particular quasicrystal has 5-fold rotational symmetry. An algorithm was written to generate arbitrarily large quasicrystal

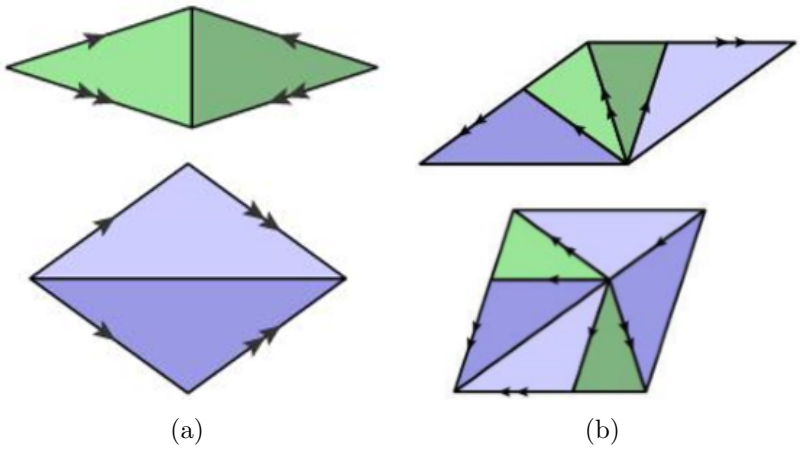

Figure 18: (a) The two rhombuses that compose the P3 tiling along with the matching rules associated of how they tile. These two rhombuses can be further broken down into four triangles (b) The decomposition of the triangles according to the matching rules [57]

patterns using the substitution method and the decomposition of the triangles according to the matching rules associated with the tiling as shown in Figure 18 [57]. The results of the algorithm is seen in Figure 19. From this, a large area quasicrystal pattern was generated and all the vertices of the tiling was taken as the location of a cylinder resulting in the pattern in Figure 20.

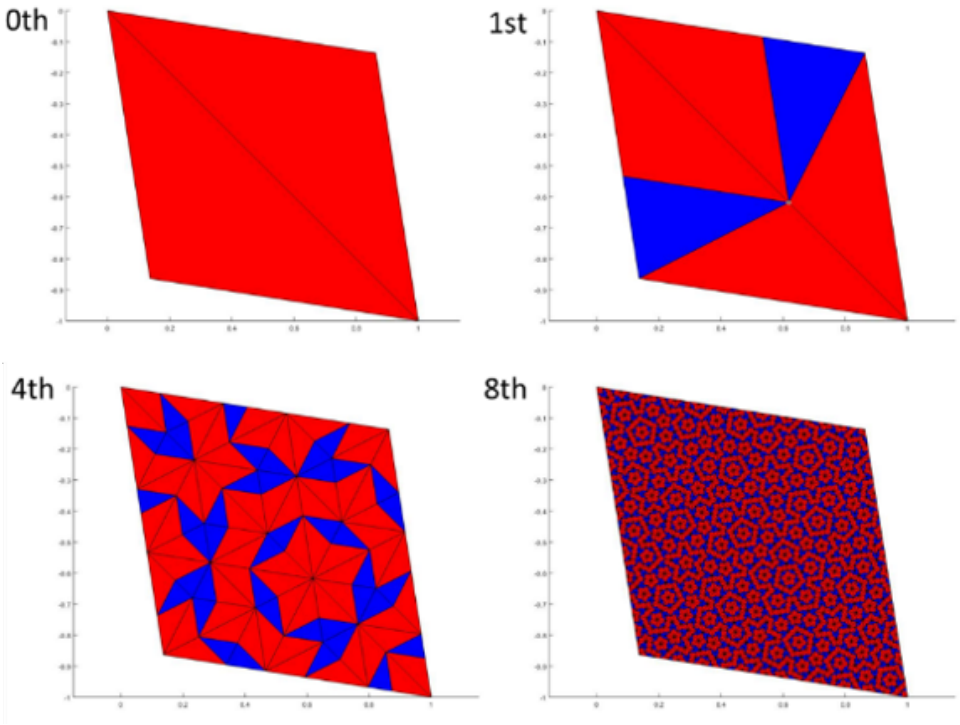

Figure 19: Generating arbitrarily dense quasicrystal patterns. Each repeating generation of decomposition generates a denser pattern

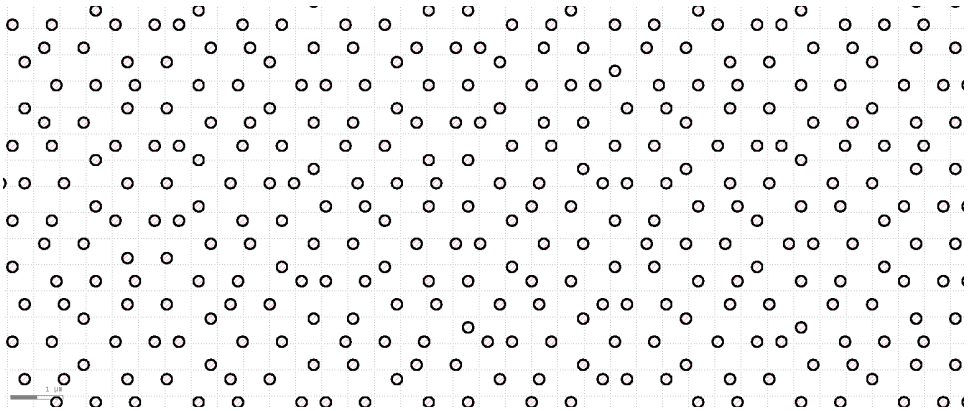

Figure 20: The final quasicrystal pattern for the metagrating. A cylinder is placed at the Penrose tiling vertices to form the pattern

4.3 Fabrication of the Metagrating

Several different types of metagratings were fabricated: 1D periodic lines and spaces, cylinders arranged in a square array, and lastly cylinders arranged in a quasicrystal pattern. All samples were fabricated on silicon substrates with thin native oxide(3 nm). A 50 nm layer of silver is thermally evaporated with a Lesker Thermal Evaporator onto the substrates with an adhesion layer of 5 nm of titanium. This will act as the metal backplane reflector. On top of this layer of silver, ZrO_2 is deposited using the low temperature UV anneal method, specifically using a two and a half hour anneal at 120°C. Different thicknesses of ZrO_2 were deposited to vary the spacing between the metal backplane and the periodic inclusions. Electron beam lithography and lift-off was used to define the gold perodic and quasiperiodic elements on top of the ZrO_2 film. The e-beam resist ZEP 520A was spun and patterned using a JEOL 6000 FSE E-beam. The pattern was developed using a bath of amyl acetate for 15 seconds. A 50 nm layer of gold with a 5 nm titanium adhesion layer was deposited via thermal evaporation, and lift-off was performed in a Remover PG bath at 80°C for two hours followed by three seconds in an ultrasonicator. Scanning electron microscope images of the resulting metagrating can be seen in Figure 21.

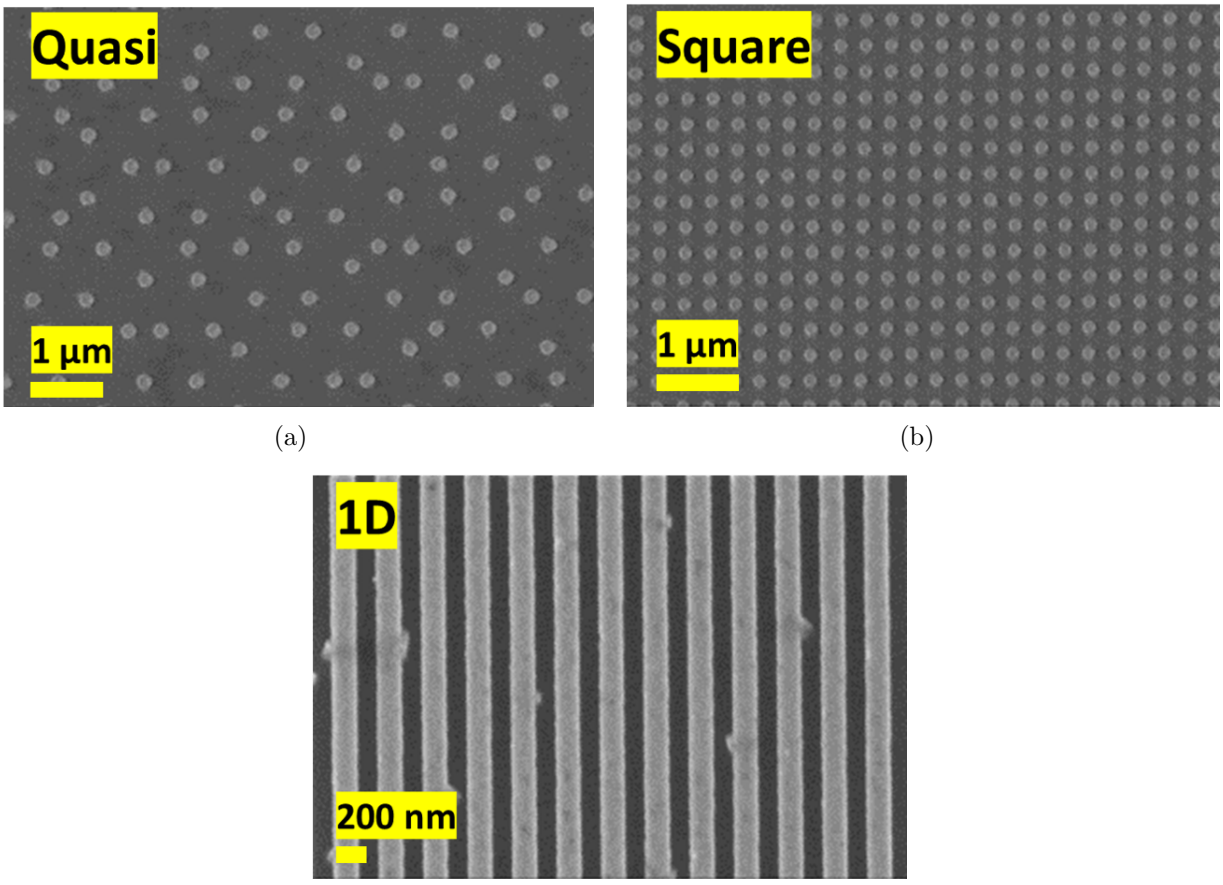

(a) (b)

(c)

Figure 21: Scanning electron microscope images of the three types of metagratings. (a) Quasicrystal (b) Square lattice (c) Periodic lines

5 Metagratings in Organic Light Emitters

The goal of this study is to use metagratings to enhance the light outcoupling efficiency for organic light emitting diodes (OLED). Rather than build a full OLED device to test, we have opted to simplify the experiment and build an optically equivalent organic light emitter (OLE). A comparision of the structure of a top emitting OLED and our metagrating enhanced OLE can be seen in Figure 22. As seen in Figure 22, the metagrating is composed of a grating element spaced above a backside reflector. We induce fluorescence by optically pumping the OLE with a violet laser. By comparing the emission from the metagrating enhanced OLEs and a reference OLE without the metagrating, we can directly see the effect of the metagrating. A comparison of OLEs with and without metagratings can be seen in Figure 23.

5.1 Fabrication of the OLE

Both reference OLEs without a metagrating and metagrating enhanced OLEs were fabricated on top of silicon substrates with thin native oxide layers. 5 nm of titanium acting as the adhension layer is first deposited, followed by 50 nm of silver with a Lesker Thermal Evaporator. The silver acts as the reflctor portion of the metagrating. The ZrO_2 is deposited via spin-coating by a sol-gel process and annealed using UV as detailed in Chapter 4. The grating portion of the metagrating is fabricated using e-beam lithography and metal-lift off as detailed in Chapter 4.

The organic layers are deposited on top by subliming materials under high vacuum in a Lesker Thermal Evaporator. The organic layers are Tris(4-carbazoyl-9-ylphenyl)amine (TCTA) and Tris(8-hydroxyquinoline)aluminum (Alq3). First, 100 nm of TCTA is deposited, followed by 50 nm of Alq3, and another 50 nm of TCTA. The emission layer is the Alq3 which is a broadband organic emitter with an emission peak in the green [59, 60].

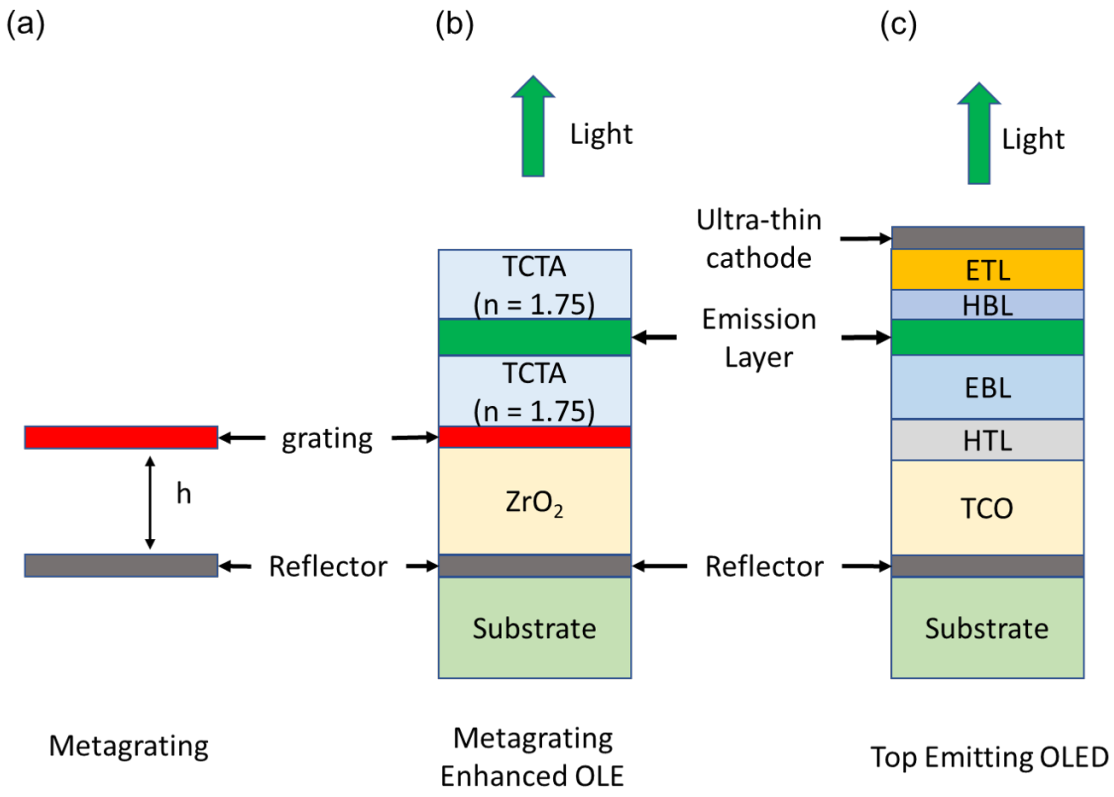

Figure 22: (a) The metagrating, which is composed of the grating element in red and a reflecting plane in grey and are spaced apart a distance h. (b) The metagrating enhanced organic light emitter stack showing the constituent layers of the device. The grating element is embedded between the ZrO_2 and the hole transporting layer TCTA. The emission layer is Alq3. (c) The structure of a top emitting OLED. From the bottom, a tranparent conducting oxide layer acting as the anode, a hole transporting layer and an electron blocking layer, the emission layer, then the hole blocking layer and electron transporting layer. Lastly the cathode, which is usually an ultrathin metal layer with high transparency.

The OLE matches the general optical structure of an OLED and so their optical performance would be very similar and key issues such as waveguide modes trapping the generated light would be present in both. The only key optical difference is that the OLE structure does not have the cathode on top, which in a top emitting OLED would be an ultrathin conductor with a very high transparency [28]. Otherwise, the two devices are almost optically identical. UV annealed ZrO_2's index of refraction is slightly lower than the mostly commonly used transparent conducting oxide of indium tin oxide (1.84 for ZrO_2 at 540 nm vs 1.87 for ITO). Also, most organic materials for OLED fabrication have very similar indexes of refraction of

1.7-1.8, so it is appropriate to treat TCTA above and below Alq3 as optically being similar to any comparable organic hole and electron transport layer sandwiching an organic emission layer [27, 31].

For a direct comparision of the effects of integrating a metagrating into an OLE, we fabricated OLEs with and without the metagrating on the same substrate. Both OLE types have the same silver mirror, layer of ZrO_2, and layers of organic material (TCTA/Alq3/TCTA). The only difference between the OLEs with and without the metagrating is the inclusion of the gold grating elements. To make comparision easy, the gold grating elements were grouped into distinct "metagrating pixels" to compare to the overall area of the substrate which are the OLEs without the metagrating.

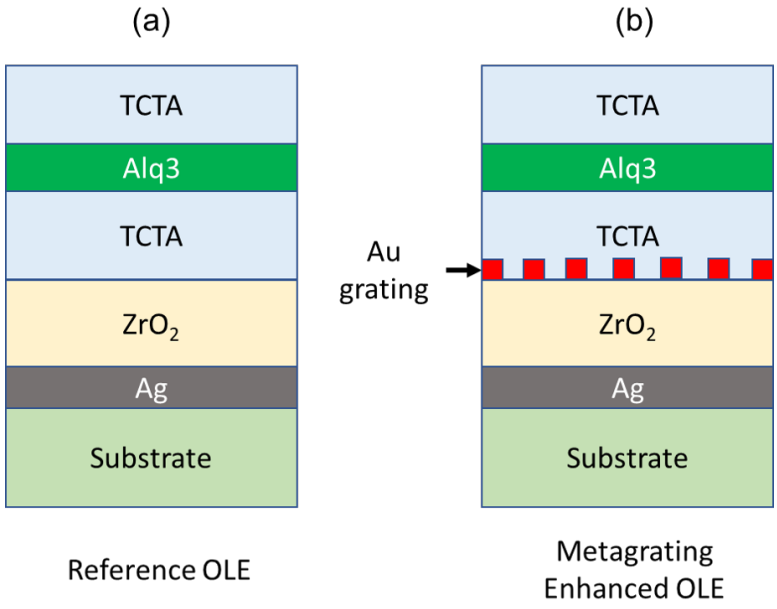

Figure 23: A comparison of OLEs (a) without and (b) with the metagrating. As can be seen, the difference between the two types of OLEs is simply a single layer of patterned gold at the interface between ZrO_2 and TCTA. The emission of the metagrating enhanced OLE will be compared to that of the reference OLE.

Several different types and sizes of metagratings were fabricated to test different parameters. Three different sizes of quasicrystals were fabricated and tested, the largest being 750 nm along the rhombus side in the tiling with a 200 nm diameter cylinder, 600 nm along the

rhombus side with a 160 nm diameter cylinder, and lastly a 375 nm along the rhombus side with a 100 nm diameter cylinder. For the periodic square array two patterns were tested: 320 nm lattice spacing with 160 nm diameter cylinders and 290 nm lattice spacing with 145 nm diameter cylinders. For the periodic lines, the two sizes tested were 320 nm period and 160 nm wide lines, and 290 nm period and 145 nm lines.

5.2 Surface Normal Emission

We used a 405 nm violet laser to stimulate fluorescence of our samples and measured the resulting surface normal emission with a camera. The emission was imaged through a series of narrow bandpass filters (FWHM 10 nm) by a ThorLabs DCC1545M monochromatic camera. A monochrome camera was chosen to simplify the emission measurement. With a monocrhome camera there is no need to worry about color when determining emission strength. The sample was kept in vacuum during these measurements to limit decay due to exposure to oxygen and moisture. The measurement setup can be seen in Figure 24.

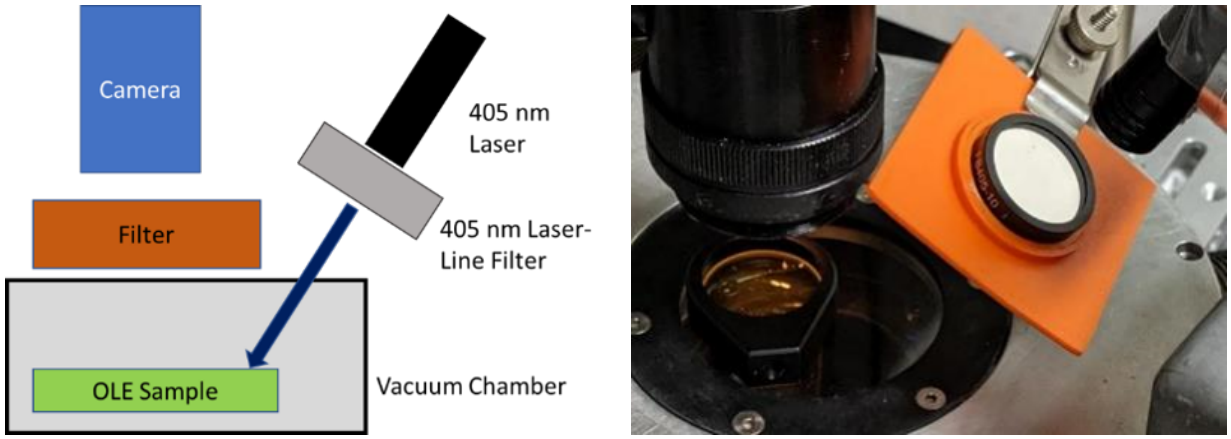

(a) (b)

Figure 24: (a) Measurement schematic. The 405 nm violet laser stimulates emission in the OLE samples which are filtered and imaged by a camera. The 405 nm laser is light is filtered by a 405 nm filter to remove any unwanted laser modes. The sample is placed inside a vacuum chamber to limit decay due to exposure to oxygen and moisture. Narrow bandpass filters (FWHM 10 nm) allows spectral analysis. A monochromatic camera images the surface normal emission. (b) Photo of actual emission measurement

To side step any nonuniformities in the laser light, one hundred images were taken, with the laser being shifted slightly in each image and a final composite image was created taking the average of the group of images. This averaged out the non-uniformity in the laser. Contained within each image were OLEs with and without the metagrating so the two conditions can be directly compared. An example of a composite image can be seen in Figure 25.

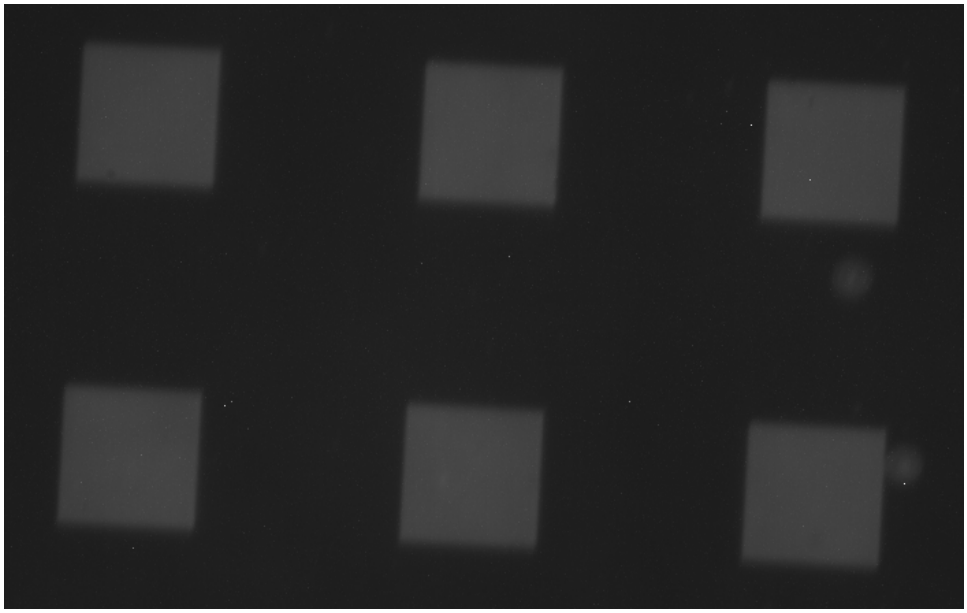

Figure 25: Example of a composite image made from 100 camera captures. By averaging through 100 camera captures with slightly different laser positions, non-uniformities in the laser can be averaged out. This image was captured through a 520 nm bandpass Filter and features six areas of a 320 nm square array metagrating. These six brighter squares are the six OLEs with metagratings. The dark regions surrounding the metagrating enhanced OLEs are where the metagrating is not present and these areas are the reference OLEs.

All comparisons presented here are between OLEs with metagratings and OLEs without metagratings. The figure of merit for these comparisons is the enhancement improvement using the following formula:

$$Improvement = \frac{Emission_{meta} - Emission_{nonmeta}}{Emission_{nonmeta}}$$

We will be comparing several different characteristics of the metagrating and their impacts on performance. The first metric we will be examining is the thickness of the ZrO_2. This

is the spacing between the reflecting metal backplane and the grating elements. Next we will compare how the various types of patterns, namely 1D lines, 2D square array, and 2D quasicrystal array. Lastly we will examine the periodicity of the different patterns.

5.2.1 Height of the Dielectric Spacer

In line with metagrating theory, the distance between the grating elements and the metal backplane is very critical to the performance of the metagrating, and this relationship is observed in our devices as well. The results can be seen in Figure 26. For all three different patterns: 1D, square, and quasicrystal, five different samples of varying thicknesswere made and the surface normal emission was measured. We tested four different ZrO_2 thicknesses: 100 nm, 120 nm, 155 nm, and 200 nm. The 155 nm sample differed slightly from the other samples in that the silver reflector layer is only 17 nm thick rather than 50 nm compared to the other samples. Previous experiments suggest while there is a degradation in performance with the thinner silver, the overall behavior is largely similar. Additionally there are two 200 nm samples. The two 200 nm samples are different due to improved expertise at fabrication with the first 200 nm sample that was fabricated having a noticeably worse quality silver reflector layer. This first layer is denoted as 200 nm** in Figure 26.

Overall as the thickness of the ZrO2 increases from 100 nm to 200 nm, the performance increases. For all three patterns, at 100 nm thickness below wavelengths of 540 nm the performance of the metagrating OLE is worse compared to the reference, though all show an enhancement as we move towards longer wavelengths. As the thickness of the ZrO_2 increases though, the performance in the shorter wavelengths begin to increase for the metagrating OLEs compared to the reference. At 120 nm, both the square and quasicrystal pattern shows a fairly uniform increase across all the wavelengths with 1D still having large wavelength spans with worse performance than reference. At 155 nm, the 1D and square show a strong enhancement between 500 nm and 540 nm while the quasicrystal shows a more uniform

enhancement. At 200 nm, all three patterns show a very distinct enhancement peak around 510 nm to 520 nm, though the quasicrystal's peak is much wider with a double peak occuring at 580 nm.

According to metagrating theory [4], the role of the spacer ZrO_2 seperating the grating and the reflector is to manipulate the number of diffraction channels the reflected light is guided into. From the results, it appears that by increasing the height of the spacer and seperating the grating the reflector more, we are coupling more light into the zeroth order diffraction channel.

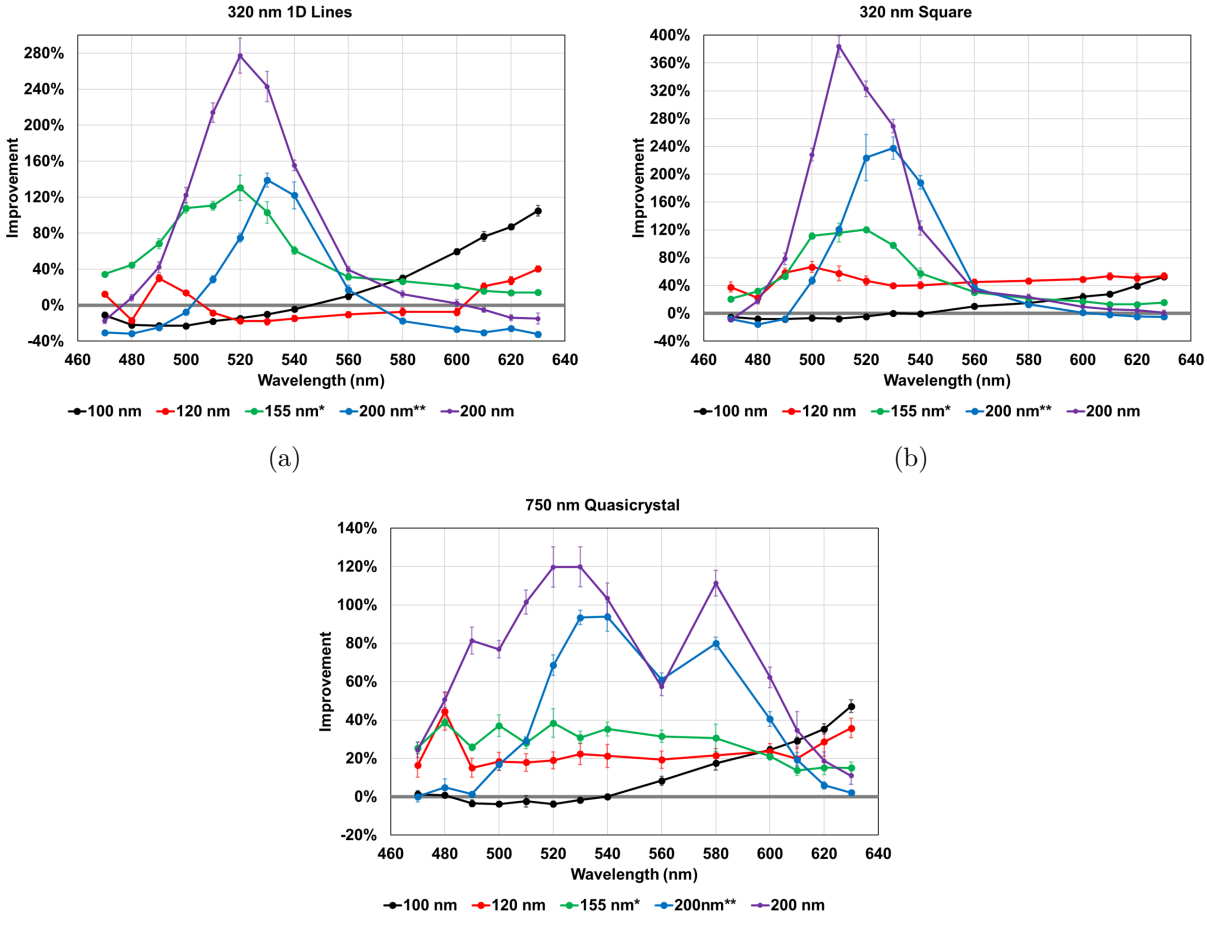

Figure 26: Variable thickness of the ZrO_2 spacer layer between the reflecting backplane and the grating elements. (a) Periodic 1D lines and spaces (b) Square array of cylinders (c) Quasicrystal array of cylinders

5.2.2 Types of Grating Pattern

Examining the performance of the different patterns at the same ZrO_2 thickness gives a couple of interesting results. For ZrO_2 at 100 nm thickness, the three patterns follow largely similar performance with the 1D pattern being slightly more exaggerated. At 120 nm thickness, the three different patterns are quite different with the square performing the best, followed by the quasicrystal, followed by the 1D pattern. The 1D pattern shows large wavelength spans where it is worse than the reference while the other two show no such behavior. At 155 nm and 200 nm thicknesses, both the square and 1D pattern outperformed the quasicrystal with a distinctly higher peak enhancement. However, at 200 nm the quasicrystal shows a second peak at 580 nm that is not present in either of the periodic patterns. Also the quasicrystal at 200 nm ZrO_2 thicknesses always out performs the reference which is not true for the two periodic patterns. In general, the quasicrystal has the least instances of performing worse than the reference across all thicknesses of ZrO_2.

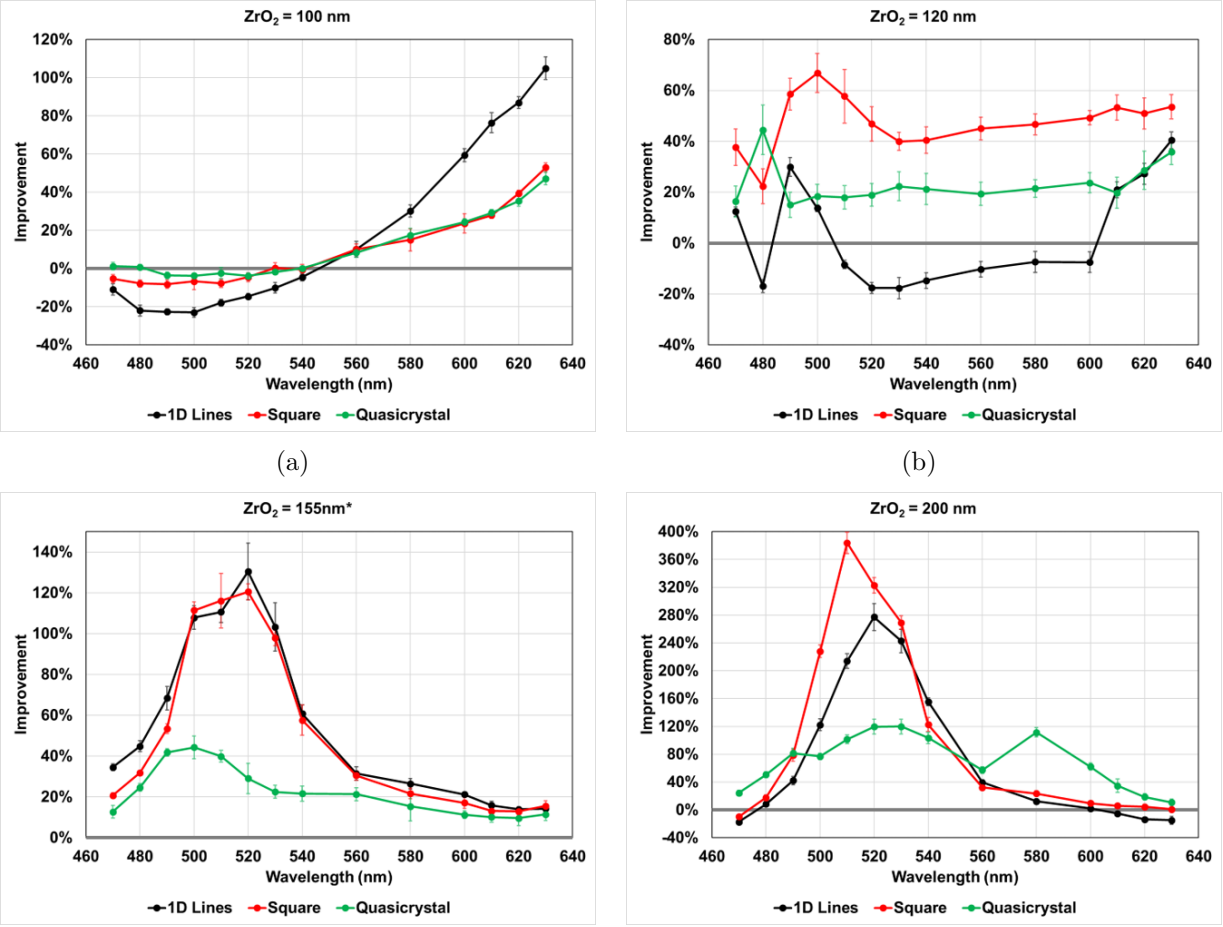

Figure 27: Comparing the different metagrating patterns at various heights of the ZrO_2 spacer (a) ZrO_2 = 100 nm thick (b) ZrO_2 = 120 nm thick (c) ZrO_2 = 155 nm thick (d) ZrO_2 = 200 nm thick

5.2.3 Periodicity Size

The results of different periodic sizings can be seen in Figure 28. All four samples plotted were fabricated on the same substrate with the same ZrO_2 thickness of 200 nm. Comparing the periodic metagratings there appears to be a couple of observable patterns. As expected, for both periodic square arrays and 1D lines, the smaller period shifts the enhancement towards to the blue. A smaller period means a resonance wavelength that is also smaller, and this is observed with the peak enhancement shifting towards narrower wavelengths. The performance of the 290 nm periodic square worsens compared to the 320 nm periodic square.

This is due to the decrease in plasmonic performance for gold at 500 nm and below. For the 1D perodic lines, the blue shift is smaller with the peak going from 530 nm for 320 nm periods to 520 nm for 290 nm periods. However, due to the smaller shift the peak enhancement is still above the 500 nm wavelength where gold stops being a good plasmonic material [61–63], and we can see that the peak enhancements are similar.

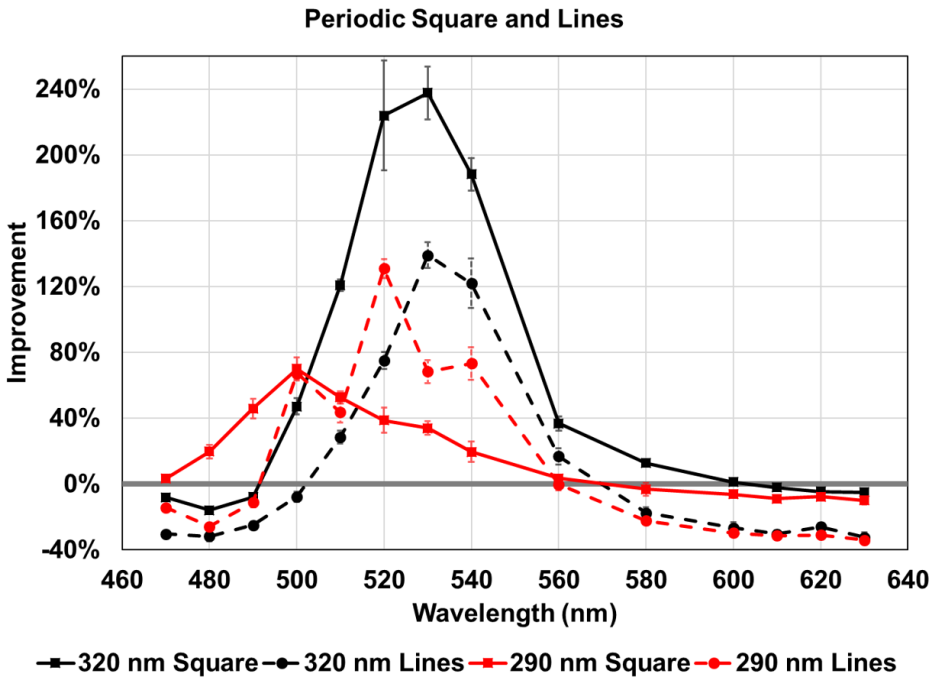

Figure 28: Comparing the periodic patterns of different periods. The samples were all fabricated on the same substrate and the thickness of the ZrO_2 is 200 nm. 320 nm and 290 nm refers to the repeating period of the structures. Square refers to a square array of cylinders which have diameters of 160 nm and 145 nm for the 320 nm period and 290 nm period structures respectively. Lines refers to a 1D periodic lines with widths of 160 nm and 145 nm for the 320 nm period and 290 nm periodic sturcutres respectively.

The results of different quasicrystal sizings can be seen in Figure 29. All three samples plotted were fabricated on the same substrate with the same ZrO_2 thickness of 155 nm. For the quasicrystals, the measurement given denoting the size of the quasicrystal refers to the length of the rhombuses which make up the quasicrystal tiling. Comparing the quasicrystal metagratings of various sizes, we can see that the spacing of the quasicrystal does not seem to make a large difference in the overall shape of the enhancement curve except at an apparent resonance frequency at 500 nm where there is a large difference between the three different

sizes. Interestingly enough the enhancement peak at 500 nm does not follow the geometry. 600 nm quasicrystals perform the best at 500 nm, followed by 375 nm, and then 750 nm. However, the 750 nm quasicrystal has the flattest enhancement curve with it outpeforming the two smaller quasicystals at wavelengths above 520 nm.

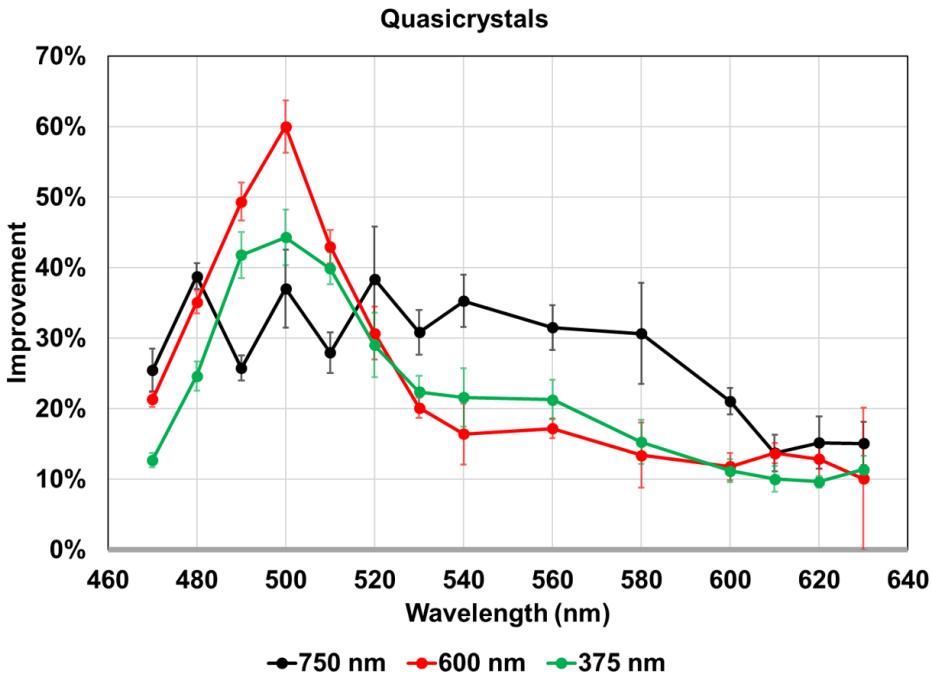

Figure 29: Comparing the quasicrystal of different sizes. All samples are on the same substrate with the thickness of the ZrO_2 being 155 nm. 750 nm, 600 nm, and 375 nm refers to the length of the rhombuses used to construct the quasicrystal. The diameters of the cylinders arranged in the quasicrystal pattern are 200 nm, 160 nm, and 100 nm for the 750, 600, and 375 nm quasicrystals respectively.

5.3 Surface Normal Reflectance

Next we measured the surface normal reflectance of the best performing OLEs which corresponds to the 200 nm thick ZrO_2. Four OLEs were measured: the reference OLE with no metagratings and three OLEs with metagratings as follows: the 320 nm periodic 1D line, the 320 nm periodic square array, and the 750 nm quasicrystal array. We used a custom built imaging spectrophotometer to measure the surface normal reflectance across the visible spectrum from 400 nm to 700 nm. We limited our analysis to the wavelength region where

we already had surface normal emission, i.e. 470 nm to 630 nm. The resulting reflectance is plotted in Figure 30. A silicon mirror was used as the reference with the known reflectance of silicon modeled in the analysis to give an absolute reflectance in Figure 30 (a) of the three metagrating enhanced OLEs along with the reference, which is labeled "Ag". Figure 30 (b)-(d) compares the relative emission enhancement to the relative reflectance change of the metagrating OLE against the reference OLE with no metagrating.

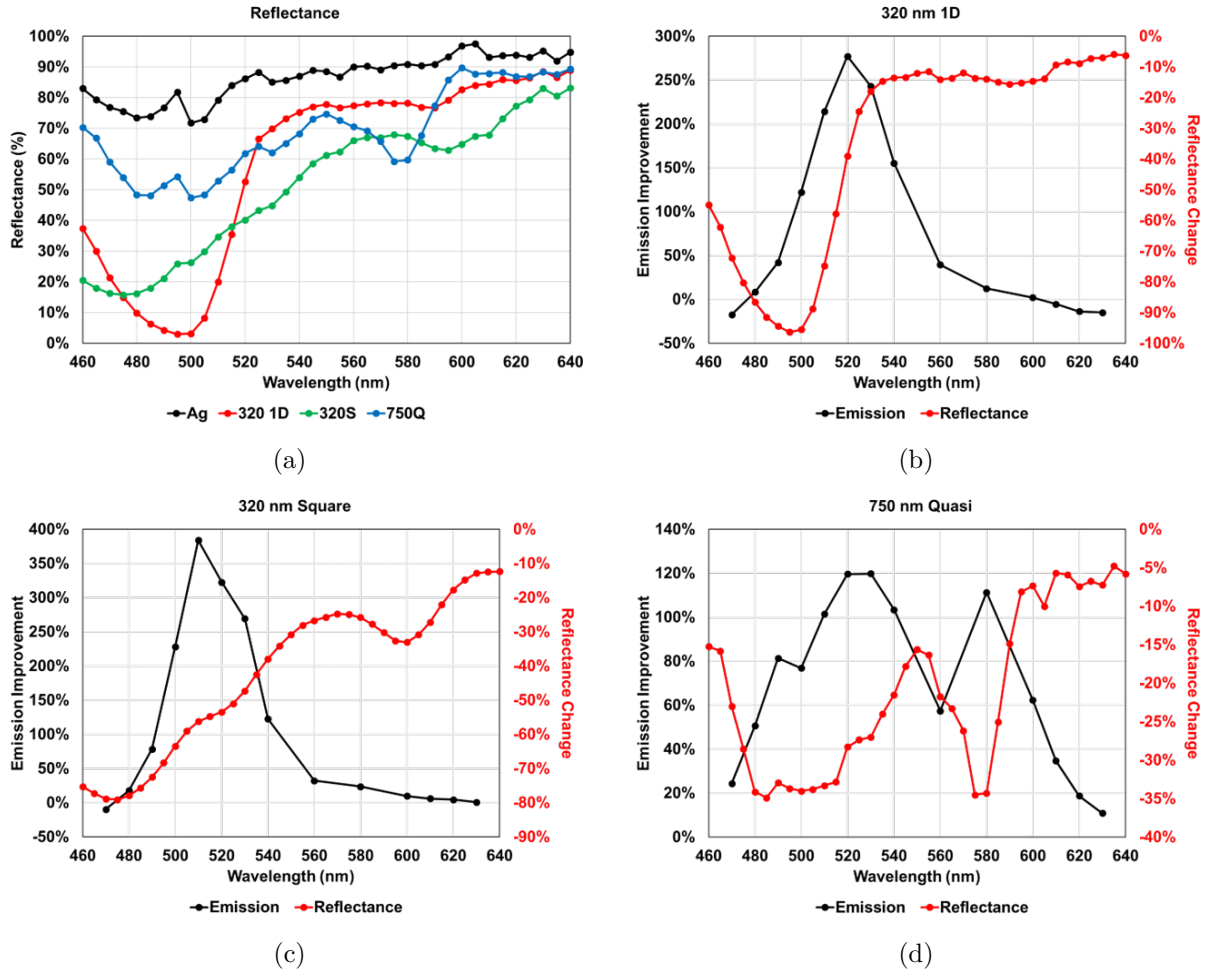

Figure 30: The surface normal reflectance of three metagrating OLEs and the reference OLE as measured by an imaging spectrophotometer. The three gratings are the 320 nm period 1D lines, 320 nm period square array of cylinders, and 750 nm quasicrystal array of cylinders. All OLEs are fabricated on the same substrate with the exact same thickness for all the layers. The ZrO_2 thickness is 200 nm. (a) the absolute reflectance of the four OLEs (b) a comparison of the relative emission enhancement of the 320 nm 1D metagrating OLE against the reference OLE in black with the relative change in reflectance (c)the same comparision for 320 nm square metagrating (d) the same for the 750 nm quasicrystal

There are two phenomenons occuring that explain the relationship between the relative reflectance and the relative emission. One is the the natural reciprocity of light. The metagrating is effective at redirecting light that would normally get trapped in waveguide modes into surface normal emission modes. When light is generated for the emission measurements, the generated light is redirected away from waveguide modes to surface normal emission. When light is surface normally incident on the sample for reflectance measurements, the normally incident light is redirected by the metagrating into waveguide modes. Thus we see the behavior that lower relative reflectance gives rise to higher relative emission. This is best observed in the quasicrystal reflectance and emission plot in Figure 30 (d). At 580 nm the relative emission spikes, and the relative reflectance dips.

The second phenomenons has to deal with the material used to make the grating element of the metagrating, namely gold. At wavelengths 500 nm and above gold is a well behaving plasmonic material meaning the real component of its relative permittivity ϵ_r' is large and negative. However, at 500 nm for gold, $-\epsilon_r' < 2$ which means that while it is plasmonic because ϵ_r' is still negative, the quality factor of the surface plasmon resonances is low and lossy [61–63]. Thus both the relative reflectance and relative emission suffer because of plasmonic loss.

5.4 Angular Dependent Emission

Lastly, we measured the angular dependent emission using an Avantes AvaSpect-2048-USB-UA spectrometer with 2.3 nm FWHM wavelength resolution connected through a fiber optic cable. The cable was mounted on a rotating stage which could swivel about the sample. A schematic of the measurement setup can be seen in Figure 31. The wavelength specific angular data shown in Figure 32, 33, and 34 was compiled by first averaging four measurements and integrating plus and minus 5 nm around the wavelength of interest to take an average. For the angular specific wavelength spectra as shown in Figure 35, this was done by taking

a nine point moving average of the raw spectrometer data resulting in a grouping of a data point every 5.2 nm of wavelength.

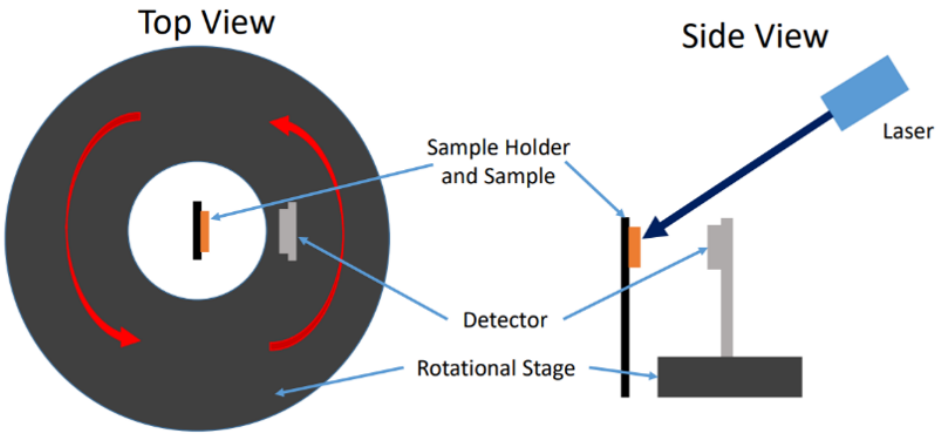

Figure 31: The setup for the anglular emission profile measurements. The OLEs are mounted in a sample holder that remains fixed in the center of a rotating stage. On the rotating stage is a fiber optic cable connected to a spectrometer set at the same vertical level as the OLEs. The exciting 405 nm laser is filtered through a 405 nm filter and impinges upon the OLE samples at an angle to avoid interaction with the rotating measurement head. Measurements are done at 10 degree intervals.

As with the reflectance measurements, four different OLEs with measured: the reference OLE with no metagrating, and three OLEs with metagratings: the 320 nm periodic 1D grating, the 320 nm square array 2D grating, and the 750 nm quasicrystal grating. The emission measured by the spectrometer has been scaled according to the surface normal emission which for this angular measurement would be 0 degrees. The angular emission for three different wavelengths are plotted for each of the three different metagrating enhanced OLEs, with the OLE with no metagrating also being plotted as a reference along with a lambertian emission pattern.

Figure 32 shows the results from the 320 nm periodic 1D grating compared to the reference OLE with no metagrating. Figure 32 (a) shows the surface normal emission improvement compared to the reference OLE. This is the emission at 0 degrees. On this plot we have highlighted three wavelengths to check the angular emission profile. We have checked at wavelength 520 nm, the highest improvement point compared to reference in Figure 32 (b).

We have also checked 560 nm which has a much lower improvement as seen in Figure 32 (c), and lastly we have checked at wavelength 620 nm where the surface normal improvement is actually worse in Figure 32 (d). All these plots in (b) - (d) have been normalized according to the 0 degree surface normal emission measurement. The black line is the reference OLE, denoted "Flat" and the red line is a lambertian emission pattern.

In Figure 32 (b) we can see that the improvement is high at all angles, not just the normal. There is a distinct peak at 0 degrees though with a second peak at 20 degrees. This suggests that these are the diffraction peaks. For 560 nm, in Figure 32 (c), the improvement is again at all angles and there is a peak at 10 degrees. From this we can deduce that different wavelengths will have different diffraction grating peaks, which matches well with how diffraction gratings should behave. Lastly, in Figure 32 (d) we see that though the metagrating OLE surface normal emission at 0 degrees is actually worse than the reference, but at higher angles the metagrating OLE outperformes the reference "flat" OLE. Again we see two distinct peaks at 30 degrees and 60 degree suggesting more diffraction peaks.

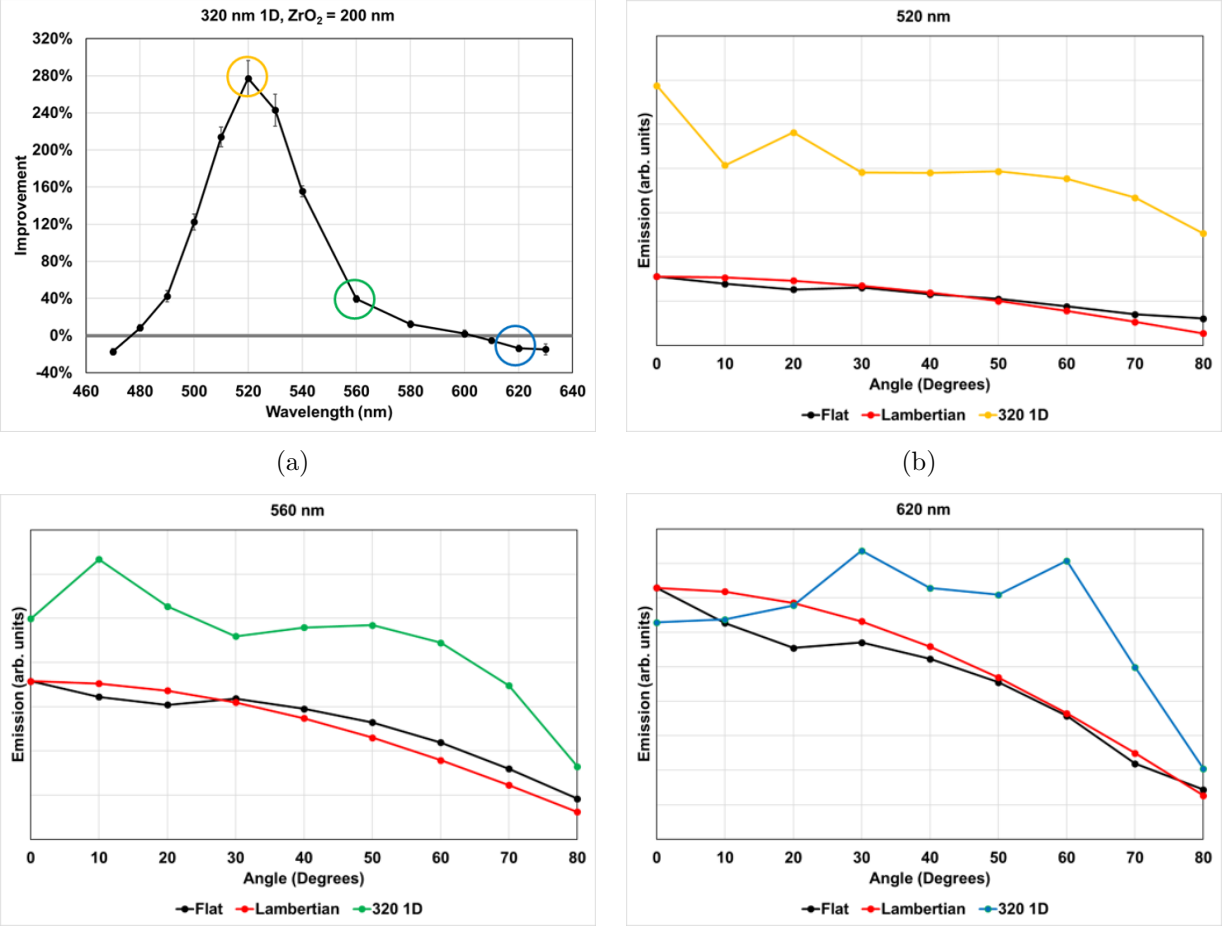

Figure 32: The angular emission profile for OLEs with the 320 nm 1D line metagrating. (a) The surface normal emission enhancement measured with the monochromatic camera. Three wavelengths are highlighted in different colors 520 nm in yellow, 560 nm in green, and 620 nm in blue. (b) The angular emission profile of the metagrating enhanced OLE at 520 nm in yellow, the reference "flat" OLE with no metagrating at 520 nm in black, and a lambertian emission pattern in red. (c) The angular emission profile at 560 nm in green and the corresponding reference in black and lambertian in red. (d) The angular emission profiles at 620 nm.

Figure 33 shows the results from the 320 nm periodic square array 2D grating compared to the reference OLE with no metagrating. As before with Figure 32, (a) shows the surface normal emission improvement compared to the reference OLE with no metagrating, while (b)-(d) shows the angular emission profile for highlighted wavelengths. For this metagrating OLE, we have again highlighted the wavelength of peak enhancement at 510 nm, a wavelength of lower enhancement at 560 nm, and lastly a wavelength where there is little to no enhancement

at 620 nm. As before with the 1D case, for the highest surface normal emission enhancement at 510 nm, we have a peak at 0 degrees followed by a peak at 20 degrees and at high angles the performance of the metagrating OLE still outperforms the reference "flat". The 560 nm angular emission profile shows a peak at 10 degrees and a flat profile extending to about 60 degrees after which it drops fairly quickly. For 620 nm, again we see that at 0 degrees the emission enhancement of the OLE is not very high, but at higher angles it outperforms the reference OLE quite a bit.

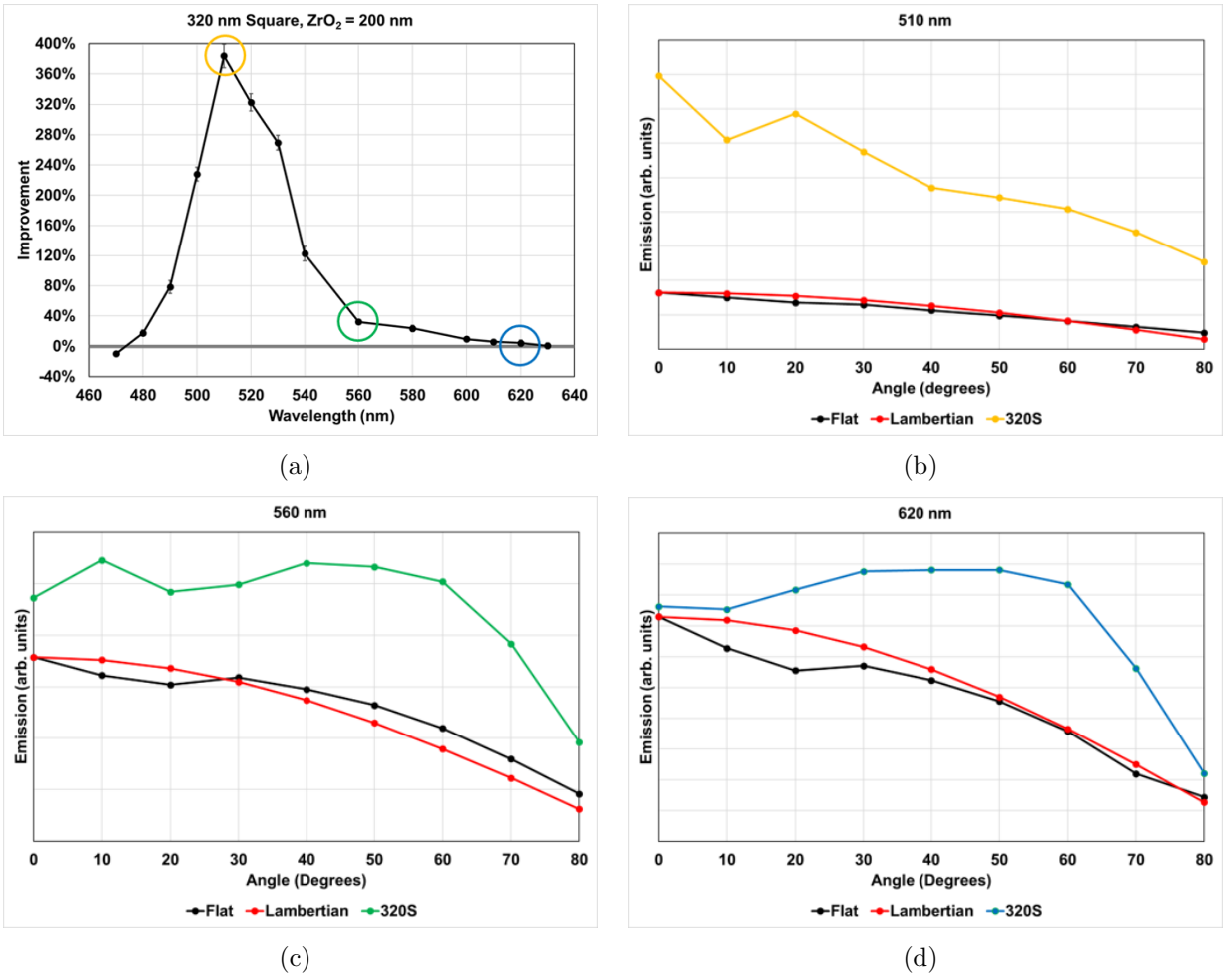

Figure 33: The angular emission profile for OLEs with the 320 nm square array metagrating. (a) The surface normal emission enhancement measured with the monochromatic camera. Three wavelengths are highlighted in different colors 510 nm in yellow, 560 nm in green, and 620 nm in blue. (b) The angular emission profile of the metagrating enhanced OLE at 510 nm in yellow, the reference "flat" OLE with no metagrating at 520 nm in black, and a lambertian emission pattern in red. (c) The angular emission profile at 560 nm in green and the corresponding reference in black and lambertian in red. (d) The angular emission profiles at 620 nm.

Figure 34 shows the resutls from the 750 nm periodic quasicrystal 2D grating compared to the reference OLE with no metagrating. Figure 34 (a) shows the surface normal emission enhancement compared to the reference OLE along with colored circles highlighting specific wavelengths at which the angular emission profile was examined. The first wavelength of interest is at 520 nm where the enhancement was highest and is highlighted in yellow and seen in (b). The metagrating OLE shows a fairly flat emission profile with until nearly 70 degrees. The key exception is a very large spike at 20 degrees. This is in contrast to the two periodic gratings seen in Figures 32 and 33 where the highest surface normal enhancement has a peak at 0 degrees when we examine the total angular emission profile. Looking at the angular profile, we can see that at 20 degrees the metagrating OLE emission is over 3.5x the reference OLE emission. At off resonance at 560 nm, we see no such strong peaks though there is a slight peak at 10 degrees and 40 degrees. At 620 nm wavelength we see no distinct peaks. At all wavelengths, we observe that the metagrating OLEs outperformance the reference at all angles.

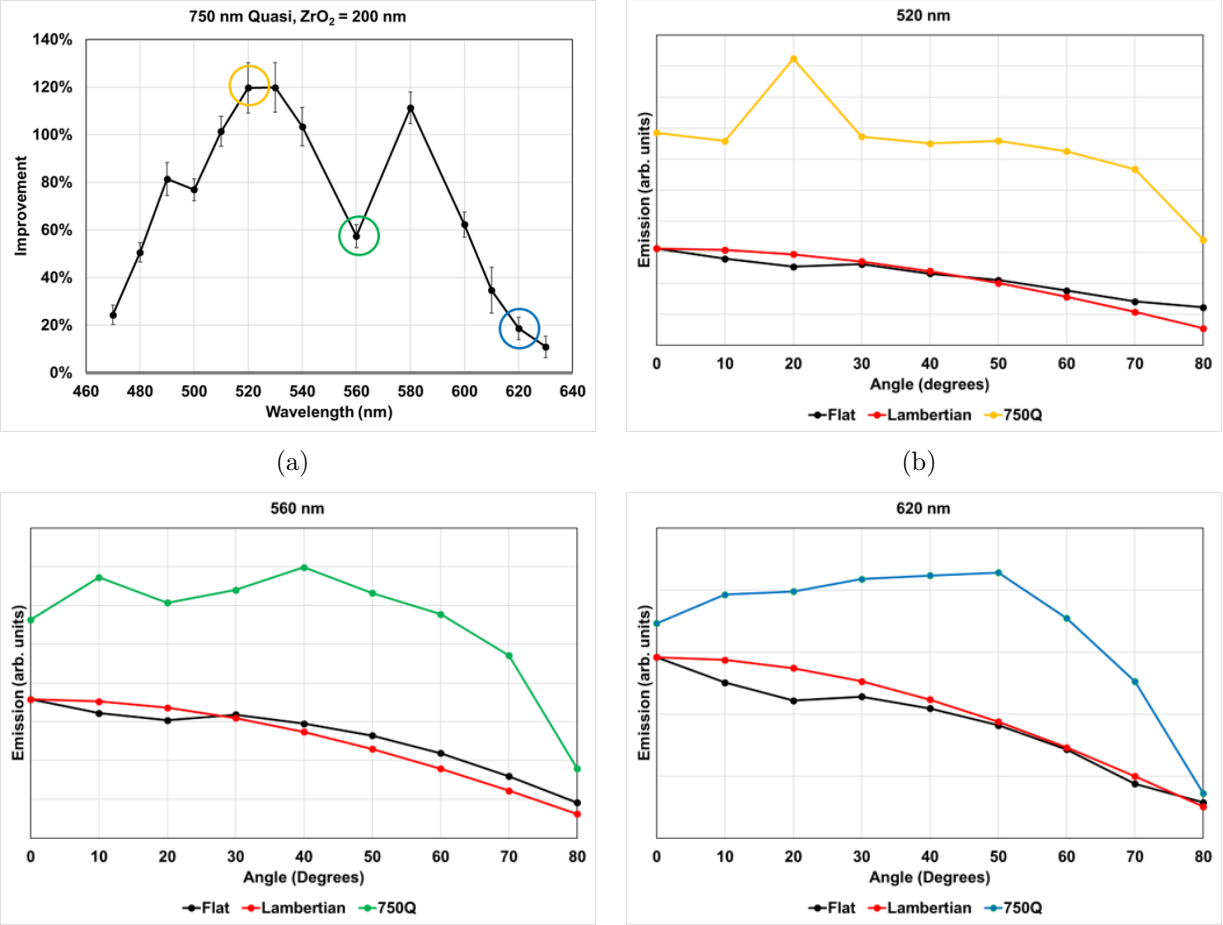

Figure 34: The angular emission profile for OLEs with the 750 nm quasicrystal array metagrating. (a) The surface normal emission enhancement measured with the monochromatic camera. Three wavelengths are highlighted in different colors 520 nm in yellow, 560 nm in green, and 620 nm in blue. (b) The angular emission profile of the metagrating enhanced OLE at 520 nm in yellow, the reference "flat" OLE with no metagrating at 520 nm in black, and a lambertian emission pattern in red. (c) The angular emission profile at 560 nm in green and the corresponding reference in black and lambertian in red. (d) The angular emission profiles at 620 nm.

From the angular emission profile for all the metagrating enhanced OLEs, we can observe a couple of details. First there are distinct peaks in the emisson profile which corresponds with the diffraction grating effect of the metagrating. As expected from diffraction grating physics, the different wavelengths have different diffraction peaks. For the two periodic structures, the strongest surface normal emission enhancement also corresponds to a large diffraction peak at 0 degrees. For the quasicrystal structure, the strongest enhancement

appears at 20 degrees off normal. For all the metagratings, the enhancement occurs at all angles and generally the angular emisson profile appears to be flatter than a lambertian emission pattern with only large decays in emission strength at large oblique angles of more than 60 degrees.

The angular emission spectra also produces some interesting results and can be seen in Figure 35, with (a) representing the spectra from the 320 nm 1D metagrating OLE, (b) representing the 320 nm square metagrating OLE, and (c) representing the 750 nm quasicrystal metagrating OLE. From this data, we can see a couple of patterns which correspond well with the anticipated behavior of these grating structures. First from the Figure 35 (a), we can see the diffraction peaks for the 1D structure. The black line representing 0 degrees and the surface normal emission, we see a large single peak from 520 to 540 nm. Then at 10 degrees in red, there are two peaks: one at 490 nm and another at 560 nm. Next at 20 degrees in yellow, there are three peaks at 485 nm, 525 nm, and 585 nm. By 30 degrees off normal, there does not to be appear to be any distinct peaks. However this matches well with diffraction grating theory which predicts that different wavelengths will react to the grating in different ways. Figure 35 (b) also shows very distinct peaks for 0, 10, and 20 degrees. The quasicrystal angular emission spectra is the most interesting as seen in (c). We can see that for all angles except for 20 degrees in yellow, the spectra is largely similar. However, 20 degrees there are two very distinct peaks and also the spectra is noticeably higher from 460 nm to 535 nm. This suggests that the light is strongly being redirected into this diffraction channel that is 20 degrees off normal.

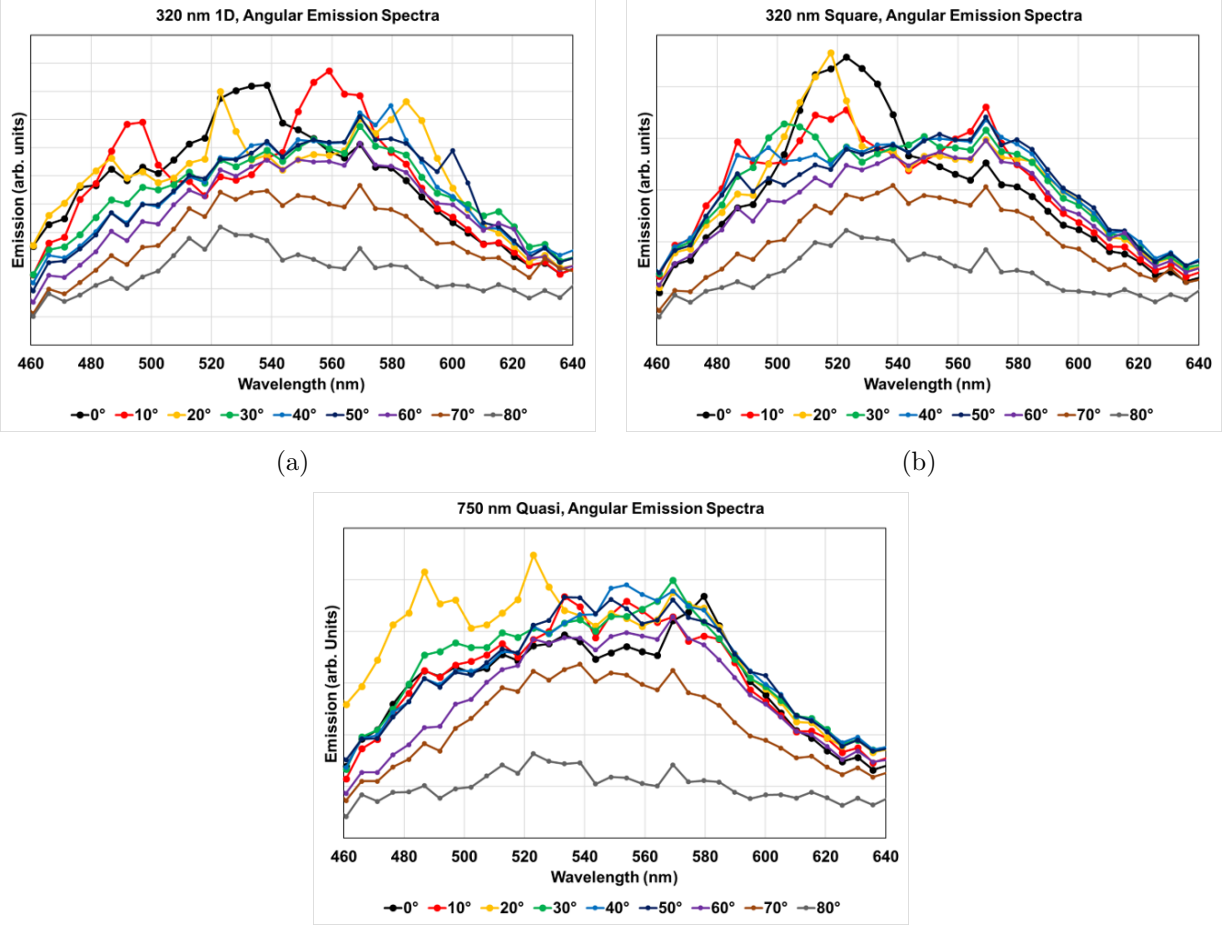

Figure 35: The angular emission spectra for three metagrating enhanced OLEs. (a) 320 nm 1D periodic lines and spaces (b) 320 nm square array of cylinders (c) 750 nm quaiscrystal array of cylinders

5.5 Discussion and Conclusion

We have demonstrated light output coupling enhancement with an integrated metagrating for a device that is optically very similar to an OLED. These results are a way forward to raise the external quantum efficiency of OLEDs by mitigating the optical losses. Three different types of grating patterns were used for our metagratings and they each offer unique benefits. 1D periodic lines offer high outcoupling efficiency and the highest degree of polarized light emission. The polarization of the light emission will be discussed in more detail in Chapter 6. 2D square array gratings offers the highest peak enhancement, though in a relatively

narrow band. This structure makes it a good fit for color specific enhancement. Quasicrystal metagratings offer the lowest enhancement, but the widest wavelength span of enhancement. Quasicrystal metagratings also generally do not perform worse than the reference. For the periodic arrays, both square and 1D lines, there is higher enhancement at the resonance frequency however at wavelengths far away from the resonance the performance can degrade compared to reference OLEs with no metasurface.

All the metagratings offer distinct usages and advantages. This method does not add much additional bulk to the overall thickness of the OLED because it only requires the addition of grating elements since top-emitting OLEDs will already feature a metal backplane as the reflecting element. In addition, the gratings feature in this work are made from gold. Possible avenues of improvement would be to replace the gold gratings with silver gratings. Silver's material properties suggest that they would be a better plasmonic material than gold, specifically at wavelengths below 500 nm [62]. The reflection vs emission data showed that gold does not work very effectively at redirecting light at wavelengths below 500 nm. This would be an issue with silver. These grating structures are also highly compatible with nanoimprint lithography. Nanoimprint lithography is a high throughput technique to reproduce nano-scale patterns from a prefabricated master template and is an avenue for large scale fabrication for commercialization.

6 Polarization Dependent Emission

One key aspect of light is the polarization, and for light emitting devices, polarization can be a very important aspect of the emission profile. For example, commercially available organic light emitting diodes (OLED) displays for televisions and mobile displays emit unpolarized light. It is imporant that the light is unpolarized because there are antireflecting layers applied to the displays that rely on controlling the polarization in a very specific way. Direct emission of polarized light is also very important. Polarized light has many applications in the fields of lighting, displays, microscopy, etc [64]. For example, polarized light for general purpose illumination has been shown to reduce glare [65, 66]. The emission and control of polarzied light has been critical for other display technologies such as liquid crystal displays [64]. Polarized light can be also used as a contrast-enhancing techinque in microscopy when imaging birefringent materials [67].

Most light sources are unpolarized and the most common way of generating polarized light has been the application of polarizers onto these sources of unpolarized light. By the very nature of these polarizers which only transmit the polarization parallel to their transmission axis, a large amount of light that is perpendicular to the transmission axis is blocked. Furthermore, the addition of polarizing films onto light sources adds complexity thickness and complexity to the manufacturing process. Direct emission of polarized light would bypass these limits.

The addition of a metagrating to enhance light emission has already been discussed the Chapter 5. In this Chapter, the polarization effects of that enhanced light emission will be discussed. We will compare the results of the three different metagrating enhanced organic light emitters (OLEs): the 1D periodic grating, the 2D square array grating, and the 2D quasicrystal array gratings in terms of their polarized light emisison.

6.1 Measurement of Polarized Emission

The measurement setup is identical to the setup described in the previous chapter to measure surface normal emission with the additional of a linear polarizer. As before, a 405 nm violet laser is used to excite fluorescence emission in the OLE samples This polarizer was rotated through three positions, 0 degrees, 45 degrees and 90 degrees and images were taken to measure the surface normal emission.

In this setup, the 0 degree polarization is aligned so as to minimize the emission of the metagrating areas and then the other polarization alignments, 45 and 90 degrees, are defined in relation to this 0 degree polarization alignment. Four types of OLEs were measured with all the OLEs being fabricated on the same substrate. The four are the reference OLE with no metagrating and the three different type of metagrating enhanced OLEs: the 1D line and space grating, the 2D square array of cylinders, and the 2D quasicrystal array of cylinders.

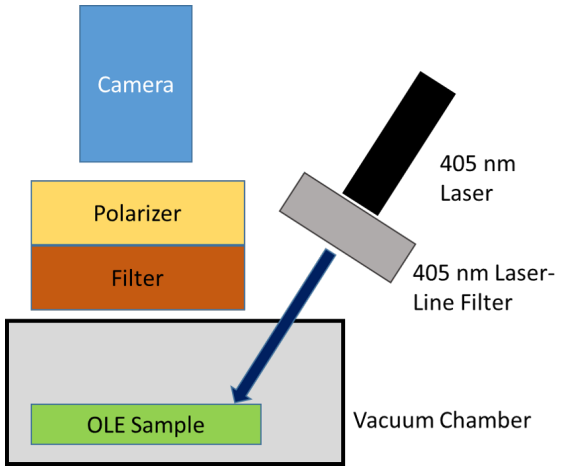

Figure 36: The scheme for the measurement of the surface normal emission enhancement of the metagrating enhanced OLEs compared to a reference OLE with no metagrating. The setup is the same as the other surface normal emission enhancement measurements as shown in Figure 24 with the exception of the inclusion of a linear polarizer layer above the wavelength bandpass filter. The linear polarizer was rotated into three different positions to measure the role of polarization in emission. 0 degrees was set at the point where the enhancement was the worst, with 45 and 90 degrees set in relation to the 0 degree baseline.

6.2 Results and Analysis

The polarization measurements showed that the enhanced light emission from the 1D metagrating pattern is strongly polarized as can be seen in Figure 37. The reference OLE with no metagrating has no polarization and no matter the orientation of the linear polarizer, the emission should be constant. Thus we will focus on comparing the enhanced emission against the reference OLE. There is a clear difference between the emission when the polarizer is aligned at 0 degrees and 90 degrees. With the polarizer aligned to 0 degrees, the emission from the metagrating OLE is worse than the reference OLE. With the polarizer aligned 90 degrees, the emission enhancement of the metagrating OLE is even higher than the case with no polarizer present. This suggest that the presence of the linear polarizer at 90 degree alignement is supressing the emission from the reference OLE with no metagrating while not strongly interacting with the emission from the metagrating enhanced OLE. This can only happen in the case where the emission from the metagrating OLE is strongly linearly polarized. Also as expected, with the polarizer set to 45 degrees, the enhancement matches well with the enhancement with no polarizer. This makes sense given that 45 degree alignment of the polarizer should suppress fifty percent of the linearly polarized light emitted by the metagrating enhanced OLE while also suppressing the reference OLE in the same way.

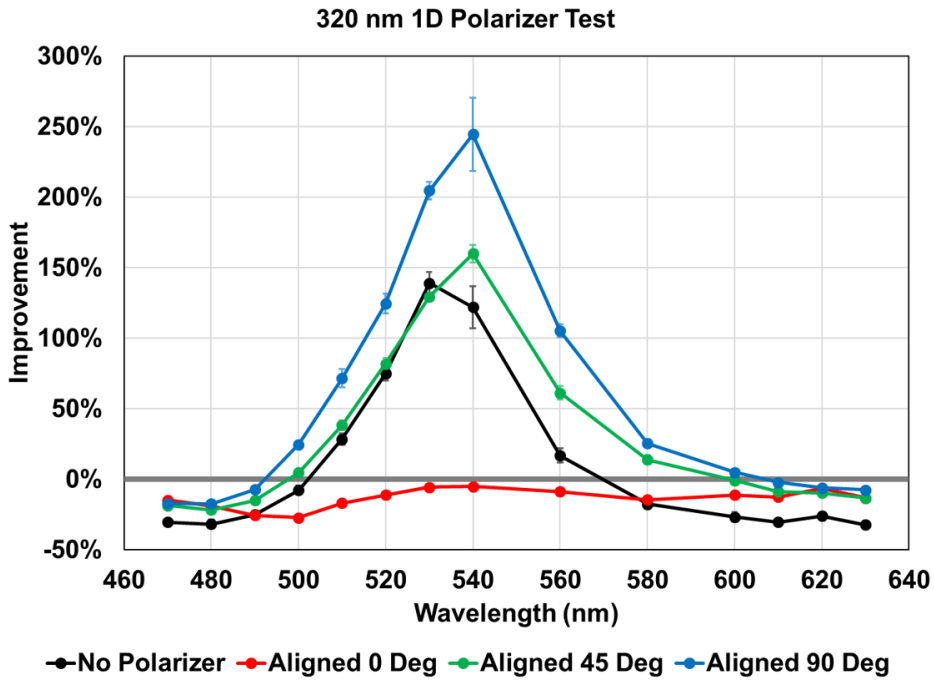

Figure 37: The surface normal emission enhancement with the addtion of a linear polarizer results for the 320 nm 1D line and space metagrating pattern. 0 degrees (in red) is set to be the baseline where the enhancement is the weakest for each metagrating at the wavelength of 530 nm. 45 degrees (in green) and 90 degrees (in blue) are set in relation to that position. The "No Polarizer" case (in black) is the when the linear polarizer is not present in the measurement setup.

The results for the polarization of the 2D square array metagrating is less clear about the polarization than the 1D metagrating and can be seen in Figure 38. The enhanced emission does appear to have some polarization to it, as there is still a difference between 0 degree polarizer alignment and 90 degree polarzier alignment. However, it is not as strong as the 1D case. If we hypothesize that the polarization of the enhanced emission should be along two distinct perpendicular axes in equal measure given the physical symmetry of the grating then we should anticipate that a 90 degree rotation in the polarizer should result in no change to the relative emission. However, this is clearly not seen. This suggest that the polarization pattern is more complicated than simply polarized along two perpendicular axes. There is still a distinct difference in the emission between the alignment of the polarizer in the three angles. So while the polarization is less than the 1D, it is still significant.

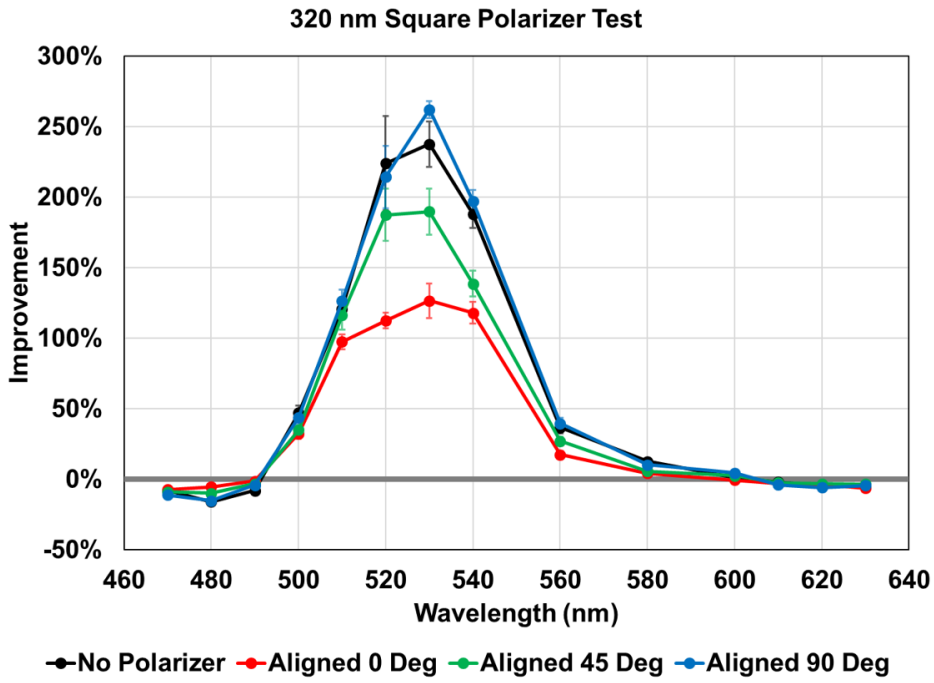

Figure 38: The surface normal emission enhancement with the addtion of a linear polarizer results for the 320 nm 2D square array of cylinders metagrating pattern. 0 degrees (in red) is set to be the baseline where the enhancement is the weakest for each metagrating at the wavelength of 530 nm. 45 degrees (in green) and 90 degrees (in blue) are set in relation to that position. The "No Polarizer" case (in black) is the when the linear polarizer is not present in the measurement setup.

The polarization results for the 2D quasicrystal array is shown in Figure 39. This metagrating enhanced OLE shows the least polarzation of the three types of metagratings used in this work with all three polarizer alignments and the case with no polarizer largely being the same. There is still minor differences but compared to the two periodic structures they are much smaller. The initial idea about using quasicrystal metagratings to reduce polarization was inspired by work on photonic crystal lasers using quasicrystal patterns. Notomi et al., showed that the emission pattern from a 10-fold symmetric quasicrystal photonic crystal laser also had a 10-fold symmetry and that it was the well matched with the reciprocal lattice of the quasicrystal in k-space. We hypothesis that the polarization may align in a similar way with select axes in real space being slightly more polarized, but the overall emission has little net polarization. Our quasicrystal was only 5-fold symmetric. It is possible that a more complicated quasicrystal with a higher amount of symmetry could offer even less

polarization.

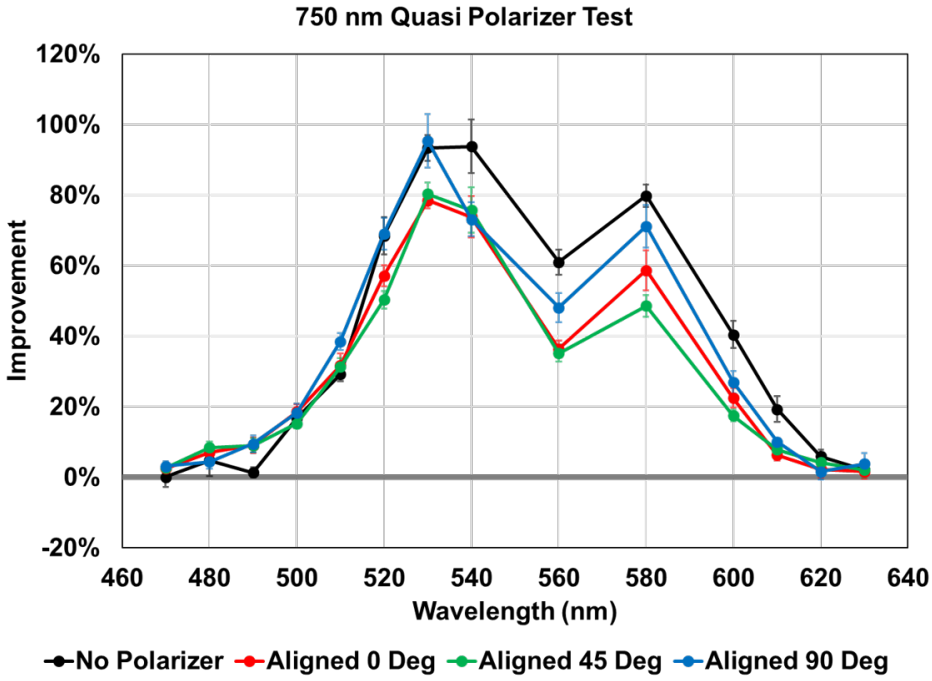

Figure 39: The surface normal emission enhancement with the addtion of a linear polarizer results for the 750 nm 2D quasicrystal array of cylinders metagrating pattern. 0 degrees (in red) is set to be the baseline where the enhancement is the weakest for each metagrating at the wavelength of 530 nm. 45 degrees (in green) and 90 degrees (in blue) are set in relation to that position. The "No Polarizer" case (in black) is the when the linear polarizer is not present in the measurement setup.

6.3 Discussion and Conclusion

Polarization is an important aspect of light emission, and as shown metagratings offer a large amount of control over the polarization of the emitted light. Metagrating integrated in OLEs not only can enhance the overall emission of the OLE, but can also be used to control the polarization of the that emitted light. 1D periodic gratings allows for the direct emission of polarized light. In contrast to a simple application of a linear polarizer to an unpolarized light source, the metagrating does not lower the overall amount of light that is emitted, it in fact enhances the light emission.

For the enhancement of light emission when polarized light is undesirable, quasicrystal meta-

gratings offers a convenient solution. For this work, we used a five-fold rotationally symmetric quasicrystal and we achieved a large emission enhancement of nearly 2x compared to references without metagratings, while keeping the polarization small. It is possible the application of quasicrystals with more rotational symmetry such as ten-fold rotationally symmetric quasicrystals can lead to even smaller polarization effects.

It is clear metagratings are well suited for light emission enhancement. While we used them primarily to control light emission in organic light emitters for comparisions to top-emitting OLEDs, they are generally applicable to all thin-film light generating technologies. The fact that their properties can be changed so dramatically with a simple rearrangement of their geometry make them appropriate for a wide variety of use cases. They can be used to enhance light emission whether you want high enhancement at select wavelengths for color specific emission, or broad enhancement for emission of white light. They can be used to control the polarization, allowing enhanced direct emission of both polarized and unpolarized light. Also their angular emission profile is also advantageous, with fairly flat responses until the angles are larger than 60 degrees off the surface normal. This would lead to displays with excellent viewing angles.

7 Appendices

7.1 Detailed Fabrication of Metasurfaces and Metagratings

This section is for fabrication details not found in the main text, future grad students and possibly post-docs this is for you. Much of this work was done on silicon substrates with native oxides. The metasurface work however was done on silicon substrates with thermally grown oxides. No matter the substrate however, they were all cleaned the same way. First they were rinsed in acetone, followed by methanol, followed by isopropol alcohol (IPA). Then

they were placed in a bath of IPA and sonicated for 5 mins to remove any debris.

For the metasurface samples, we immediately began the e-beam process while the metagrating samples had further processing. The metagrating samples required the deposition of the silver and a layer of ZrO_2 before the e-beam process. We first deposited a 5 nm layer of titanium as an adhesion layer for the silver, before depositing 50 nm of silver. As it turns out if you deposit silver directly on the silicon/native oxide substrates they will be destroyed in the e-beam process if it is too thick. 17 nm of silver was found to survive while 22 nm of silver was found to not survive. This was solved by simply depositing that titanium adhesion layer. All the metal deposition was done by thermal evaporation in a Lesker Thermal Evaporation.

Next is the deposition of the ZrO_2. ZrO_2 was chosen as the dielectric because it was compatible with ZEP 520A, the e-beam resist we used. We tried two other dielectrics but they did not work. Commercially availabe spin-on-glass from Futurex which had a low annealing temperature and a good index of refraction had the problem that ZEP 520A would not adhere to it. The low temperature ZnO sol-gel that was used in the photodetector work also did not work. ZEP 520A would adhere to it, but the resulting film did not develop after e-beam exposure and took on a shiny and metallic look. Possibly this is due to the ZnO being crystalline and the ZrO_2 being amorphous.

The sol-gel precursor solution for ZrO_2 was prepared by mixing Zirconium(IV) Chloride and Zirconium(IV) isopropoxide isopropanol complex into 2-Methoxyethanol. All the chemical were purchased from Sigma Aldrich. The exact proportions are 291.3 mg of ZrCl4 and 484.6 mg for Zr-isopropoxide to 5 mL of 2-Methoxyethanol. This can obviously be scaled to make as much or as little as one desires. The precursors were stored in a nitrogen glove box and all the mixing and preperation of the sol-gel solution is also done in the nitrogen glove box. Solutions were left stir using magnetic stir-rods at least overnight before they were used to make the films.

The ZrO_2 films were deposited by taking the precursor solution and spin-coating them onto the substrates with the silver already deposited upon them. The ZrO_2 deposition was done immediately after the silver deposition so to minimize the time silver could oxidize. The spin-coating was done inside a nitrogen glove box. Plastic syringes were used to draw the solution and it was filtered through a 0.2 micron PTFE filter when depositing the solution on the substrates. They were spin coated at 1000 RPM for 60 seconds with a ramp of 1000 RPM/sec using a Laurel spin-coater. Then they were annealed on a 100 °C hotplate inside the nitrogen glove box. This was followed by a two and half hour anneal at 120 °C while being exposed to UV light inside a Novascan PSD-UVT. The UV anneal was done in ambient. The thickness of the resulting film can be fairly variable, but it is possible to control the thickness by adjusting either the density of the precursor solution or the speed of the spin-coating.

The e-beam process for both the metasurface and metagrating are largely the same. ZEP 520A is the resist used. This is a faster resist than PMMA, requiring less exposure time to get the same results. The ZEP 520A was diluted with anisole in a ratio of 1:2::ZEP:anisole. The deposition of the diluted resist was done with a plastic syringe through a 0.2 micron PTFE filter. The spin-coating recipe is as follows: 500 RPM for 5 seconds with a ramp of 100 RPM/sec, followed by 1000 RPM for 60 seconds with a ramp of 1000 RPM/sec. The resulting films should be about 120 nm thick. It is important to not have resist that is too much thicker than 2X to 3X times the thickness of one's eventual features when doing deposition and lift-off to make metal features. If the resist is too thick, it is hard to get the correct amount of metal into the narrow resist openings.

The e-beam lithography was done in a JEOL 6000 FSE. Dose-testing was done to develop optimal exposure levels and this will differ for different e-beam lithography systems. The development of the exposed samples was done by dropping the samples into a bath of amyl acetate for 15 seconds and then rinsing the samples in DI water to wash off the developer.

Metal was then deposited using a thermal evaporator. For both the metasurface and metagrating, gold was used, 40 nm and 50 nm respectively. However a 5 nm layer of titanium was always deposited first.

Lift-off was done by submerging the samples into a heated bath of Remover PG from MicroChem at 80 °C. For the metasurface samples which had no silver, the bath lasted for four hours and was followed by a rinse with DI water to wash off the lifted-off metal. It is important to use a rinse rather than a dip because the lifted off metal will not be correctly removed if using a dip leading to re-adherence of the lifted off metal. For the metagrating samples, Remover PG actually degrades the silver. The ZrO_2 protects the silver somewhat, but to maintain better quality reflectors, a 2 hour bath was used instead, followed by a 5 second burst of ultrasonication in the Remover PG bath to help lift-off. In general if the metal is not removed by simply swirling the sample around in the Remover PG bath, using a quick burst of ultrasonication usually removes any excess metal. The metagrating samples should not be washed with DI water to clean the Remover PG off the samples. They should instead by washed with isopropol alcohol. Water causes the silver to form cracks. This might be due to the temperature difference between the water and the heated Remover PG, but IPA does not cause that same cracking.

7.2 Calculation of Error in Surface Normal Emission Measurements

All the plots for surface normal emission enhancement contain error bars associated with the measurement.There are other sources of error such as variation in fabrication and damage to the gratings and silver back reflector, but the source of error we will be focused on will be from the imaging and collection of the surface emission data. For these measurements, there is a light intensity value associated with each pixel of an image. To minimize the impact of

any aberrations of the laser spot on the data, we take a hundred images and average them. Variation in how the laser is swept across the sample is therefore also captured in this error calculation.

After the images are composited into an averaged result, we draw six sample boxes around the OLEs with metagratings, actively avoiding fabrication errors that are visible in the image and combine all of these data points into one large sample, which is named Meta Sample. The same process is applied to gather the reference OLE into a Non-Meta Sample. The Meta Sample and Non-Meta Sample are single dimensional arrays of light intensity values. The purpose of these samples, and any sample, is to accurately represent the population; however, with every sample there is a standard deviation and standard error. Standard deviation measures the variation/variability from the mean and standard error measures how far away the sample mean is away from the true mean, which is the population mean.

Using the formulas in Equations 7.2.1 and 7.2.2 we calculate the standard deviation followed by the standard error of both the Non-Meta Sample and Meta Sample. It is important to remember that when data is used in calculations that the standard error propagates. Standard error propagation can be calculated by using the formula in Equation 7.2.3. In Equation 7.2.3 "x" represents the equation for calculating the emission enhancement, "a" represents the Meta sample, and "b" represents the Non-Meta sample. Finally we have our total surface normal emission enhancement standard error which is what is plotted as our error bars.

$$\sigma = \sqrt{\frac{\sum_{i=1}^{n}(x_i - \bar{x})^2}{n-1}} \tag{7.2.1}$$

$$(\sigma_{\bar{x}}) = \frac{\sigma}{\sqrt{n}} \tag{7.2.2}$$

$$\sigma_x^2 = (\frac{\delta x}{\delta a})^2 \sigma_a^2 + (\frac{\delta x}{\delta b})^2 \sigma_b^2 \tag{7.2.3}$$

References

[1] Shengyuan Chang, Xuexue Guo, and Xingjie Ni. Optical Metasurfaces: Progress and Applications. *Annu. Rev. Mater. Res*, 48724(1):1–7, 2018.

[2] Christopher L. Holloway, Edward F. Kuester, Joshua A. Gordon, John O'Hara, Jim Booth, and David R. Smith. An overview of the theory and applications of metasurfaces: The two-dimensional equivalents of metamaterials. *IEEE Antennas and Propagation Magazine*, 54(2):10–35, 2012.

[3] Nasim Mohammadi Estakhri and Andrea Alù. Recent progress in gradient metasurfaces. *Journal of the Optical Society of America B*, 33(2):A21, feb 2016.

[4] Younes Ra'di, Dimitrios L. Sounas, and Andrea Alù. Metagratings: Beyond the Limits of Graded Metasurfaces for Wave Front Control. *Physical Review Letters*, 119(6):067404, aug 2017.

[5] Verena Neder, Younes Ra'Di, Andrea Alù, and Albert Polman. Combined Metagratings for Efficient Broad-Angle Scattering Metasurface. *ACS Photonics*, 6(4):1010–1017, 2019.

[6] David Sell, Jianji Yang, Sage Doshay, Rui Yang, and Jonathan A. Fan. Large-Angle, Multifunctional Metagratings Based on Freeform Multimode Geometries. *Nano Letters*, 17(6):3752–3757, 2017.

[7] Vladislav Popov, Marina Yakovleva, Fabrice Boust, Jean-Luc Pelouard, Fabrice Pardo, and Shah Nawaz Burokur. Designing Metagratings via Local Periodic Approximation: From Microwaves to Infrared. *Physical Review Applied*, 11(4):044054, apr 2019.

[8] Sandro F. Tedde, Johannes Kern, Tobias Sterzl, Jens Fürst, Paolo Lugli, and Oliver Hayden. Fully spray coated organic photodiodes. *Nano Letters*, 9(3):980–983, 2009.

[9] Kang-Jun Baeg, Maddalena Binda, Dario Natali, Mario Caironi, and Yong-Young Noh. Organic Light Detectors: Photodiodes and Phototransistors. *Advanced Materials*, 25(31):4267–4295, aug 2013.

[10] Zongyou Yin, Hai Li, Hong Li, Lin Jiang, Yumeng Shi, Yinghui Sun, Gang Lu, Qing Zhang, Xiaodong Chen, and Hua Zhang. Single-Layer MoS 2 Phototransistors. *ACS Nano*, 6(1):74–80, jan 2012.

[11] Thomas Mueller, Fengnian Xia, and Phaedon Avouris. Graphene photodetectors for high-speed optical communications. *Nature Photonics*, 4(5):297–301, 2010.

[12] Fengnian Xia, Thomas Mueller, Yu-ming Lin, Alberto Valdes-Garcia, and Phaedon Avouris. Ultrafast graphene photodetector. *Nature Nanotechnology*, 4(12):839–843, dec 2009.

[13] Marco Furchi, Alexander Urich, Andreas Pospischil, Govinda Lilley, Karl Unterrainer, Hermann Detz, Pavel Klang, Aaron Maxwell Andrews, Werner Schrenk, Gottfried Strasser, and Thomas Mueller. Microcavity-integrated graphene photodetector. *Nano Letters*, 12(6):2773–2777, 2012.

[14] Vivian E. Ferry, Marc A. Verschuuren, Hongbo B. T. Li, Ewold Verhagen, Robert J. Walters, Ruud E. I. Schropp, Harry A. Atwater, and Albert Polman. Light trapping in ultrathin plasmonic solar cells. *Optics Express*, 18(S2):A237, 2010.

[15] K. R. Catchpole and A. Polman. Design principles for particle plasmon enhanced solar cells. *Applied Physics Letters*, 93(19):2006–2009, 2008.

[16] Harry A. Atwater and Albert Polman. Plasmonics for improved photovoltaic devices. *Nature Materials*, 9(10):865–865, 2010.

[17] Peter Bermel, Chiyan Luo, Lirong Zeng, Lionel C. Kimerling, and John D. Joannopoulos. Improving thin-film crystalline silicon solar cell efficiencies with photonic crystals. *Optics Express*, 15(25):16986, 2007.

[18] Christopher L. Holloway, Mohamed A. Mohamed, Edward F. Kuester, and Andrew Dienstfrey. Reflection and transmission properties of a metafilm: With an application to a controllable surface composed of resonant particles. *IEEE Transactions on Electromagnetic Compatibility*, 47(4):853–865, 2005.

[19] N. Yu, P. Genevet, M. A. Kats, F. Aieta, J.-P. Tetienne, F. Capasso, and Z. Gaburro. Light Propagation with Phase Discontinuities: Generalized Laws of Reflection and Refraction. *Science*, 334(6054):333–337, oct 2011.

[20] Carl Pfeiffer and Anthony Grbic. Bianisotropic metasurfaces for optimal polarization control: Analysis and synthesis. *Physical Review Applied*, 2(4):1–11, 2014.

[21] Francesco Monticone, Nasim Mohammadi Estakhri, and Andrea Alù. Full Control of Nanoscale Optical Transmission with a Composite Metascreen. *Physical Review Letters*, 110(20):203903, may 2013.

[22] Nasim Mohammadi Estakhri and Andrea Alù. Wave-front Transformation with Gradient Metasurfaces. *Physical Review X*, 6(4):041008, oct 2016.

[23] Nasim Mohammadi Estakhri, Christos Argyropoulos, and Andrea Alù. Graded metascreens to enable a new degree of nanoscale light management. *Philosophical Transactions of the Royal Society A: Mathematical, Physical and Engineering Sciences*, 373(2049):20140351, aug 2015.

[24] L. Jay Guo. Nanoimprint lithography: Methods and material requirements. *Advanced Materials*, 19(4):495–513, feb 2007.

[25] Yoshimasa Sugimoto, Masanobu Iwanaga, and Hideki T Miyazaki. Nanoimprint Lithography for the Fabrication of Metallic Metasurfaces. In *Micro- and Nanophotonic Technologies*, pages 269–290. Wiley-VCH Verlag GmbH & Co. KGaA, Weinheim, Germany, mar 2017.

[26] Masanobu Iwanaga. Large-area metasurfaces produced with nm precision by UV nanoimprint lithography. In *2016 Progress in Electromagnetic Research Symposium (PIERS)*, volume 3, pages 1857–1861. IEEE, aug 2016.

[27] Qing Dong Ou, Lei Zhou, Yan Qing Li, Su Shen, Jing De Chen, Chi Li, Qian Kun Wang, Shuit Tong Lee, and Jian Xin Tang. Extremely efficient white organic light-emitting diodes for general lighting. *Advanced Functional Materials*, 24(46):7249–7256, dec 2014.

[28] Simone Hofmann, Michael Thomschke, Björn Lüssem, and Karl Leo. Top-emitting organic light-emitting diodes. *Optics Express*, 19(S6):A1250, nov 2011.

[29] Yutaro Tachibana, Martin Kaltenbrunner, Mari Koizumi, Naoji Matsuhisa, Wakako Yukita, Peter Zalar, Hiroaki Jinno, Takao Someya, Hiroki Kitanosako, and Tomoyuki Yokota. Ultraflexible organic photonic skin. *Science Advances*, 2(4):e1501856, 2016.

[30] Rico Meerheim, Mauro Furno, Simone Hofmann, Björn Lüssem, and Karl Leo. Quantification of energy loss mechanisms in organic light-emitting diodes. *Applied Physics Letters*, 97(25):253305, dec 2010.

[31] Amin Salehi, Xiangyu Fu, Dong Hun Shin, and Franky So. Recent Advances in OLED Optical Design. *Advanced Functional Materials*, 29(15):1–21, 2019.

[32] Leiming Wang, Jun Amano, and Po-chieh Hung. Simulating Plasmon Effect in Nanostructured OLED Cathode Using COMSOL Multiphysics. *Proceedings of the 2015 COMSOL Conference*, pages 1–6, 2015.

[33] Ds Mehta and Kanchan Saxena. Light out-coupling strategies in organic light emitting devices. *Proc. ASID-06*, 2(2):198–201, 2006.

[34] Young Rag Do, Yoon Chang Kim, Young Woo Song, and Yong Hee Lee. Enhanced light extraction efficiency from organic light emitting diodes by insertion of a two-dimensional photonic crystal structure. *Journal of Applied Physics*, 96(12):7629–7636, 2004.

[35] Wooram Youn, Jinhyung Lee, Minfei Xu, Rajiv Singh, and Franky So. Corrugated sapphire substrates for organic light-emitting diode light extraction. *ACS Applied Materials and Interfaces*, 7(17):8974–8978, 2015.

[36] Jörg Frischeisen, Bert J. Scholz, Benedikt J. Arndt, Tobias D. Schmidt, Robert Gehlhaar, Chihaya Adachi, and Wolfgang Brutting. Strategies for light extraction from surface plasmons in organic light-emitting diodes. *Journal of Photonics for Energy*, 1(1):011004, jan 2011.

[37] Jörg Frischeisen, Quan Niu, Alaa Abdellah, Jörg B. Kinzel, Robert Gehlhaar, Giuseppe Scarpa, Chihaya Adachi, Paolo Lugli, and Wolfgang Brütting. Light extraction from surface plasmons and waveguide modes in an organic light-emitting layer by nanoimprinted gratings. *Optics Express*, 19(S1):A7, jan 2011.

[38] Chien Yu Chen, Wei Kai Lee, Yi Jiun Chen, Chun Yang Lu, Hoang Yan Lin, and Chung Chih Wu. Enhancing Optical Out-Coupling of Organic Light-Emitting Devices with Nanostructured Composite Electrodes Consisting of Indium Tin Oxide Nanomesh and Conducting Polymer. *Advanced Materials*, 27(33):4883–4888, 2015.

[39] C. Liu, V. Kamaev, and Z. V. Vardeny. Efficiency enhancement of an organic light-emitting diode with a cathode forming two-dimensional periodic hole array. *Applied Physics Letters*, 86(14):1–3, 2005.

[40] Carl Pfeiffer and Anthony Grbic. Metamaterial Huygens' Surfaces: Tailoring Wave Fronts with Reflectionless Sheets. *Physical Review Letters*, 110(19):197401, may 2013.

[41] Ji-Seon Kim, Peter K. H. Ho, Neil C. Greenham, and Richard H. Friend. Electroluminescence emission pattern of organic light-emitting diodes: Implications for device efficiency calculations. *Journal of Applied Physics*, 88(2):1073–1081, jul 2000.

[42] Xin Xu, Hoyeong Kwon, Brian Gawlik, Nasim Mohammadi Estakhri, Andrea Alù, S.V. Sreenivasan, and Ananth Dodabalapur. Enhanced Photoresponse in Metasurface-Integrated Organic Photodetectors. *Nano Letters*, 18(6):3362–3367, jun 2018.

[43] Nasim Mohammadi Estakhri and Andrea Alù. Manipulating optical reflections using engineered nanoscale metasurfaces. *Physical Review B*, 89(23):235419, jun 2014.

[44] Marc Ramuz, Lukas Bürgi, Carsten Winnewisser, and Peter Seitz. High sensitivity organic photodiodes with low dark currents and increased lifetimes. *Organic Electronics*, 9(3):369–376, jun 2008.

[45] Xilan Liu, Hangxing Wang, Tingbin Yang, Wei Zhang, I-Fan Hsieh, Stephen Z.D. Cheng, and Xiong Gong. Solution-processed near-infrared polymer photodetectors with an inverted device structure. *Organic Electronics*, 13(12):2929–2934, dec 2012.

[46] Thelese Ru Bao Foong, Samarendra Pratap Singh, Prashant Sonar, Zi-En Ooi, Khai Leok Chan, and Ananth Dodabalapur. ZnO layers for opto-electronic applications from solution-based and low-temperature processing of an organometallic precursor. *Journal of Materials Chemistry*, 22(39):20896, 2012.

[47] Alexander L. Ayzner, Christopher J. Tassone, Sarah H. Tolbert, and Benjamin J. Schwartz. Reappraising the Need for Bulk Heterojunctions in Polymer - Fullerene Photovoltaics: The Role of Carrier Transport in All-Solution-Processed P3HT/PCBM Bilayer Solar Cells. *The Journal of Physical Chemistry C*, 113(46):20050–20060, nov 2009.

[48] Lingliang Li, Fujun Zhang, Jian Wang, Qiaoshi An, Qianqian Sun, Wenbin Wang, Jian Zhang, and Feng Teng. Achieving EQE of 16,700% in P3HT:PC71BM based photodetectors by trap-assisted photomultiplication. *Scientific Reports*, 5(1):9181, aug 2015.

[49] Bernd Ebenhoch, Stuart A.J. Thomson, Kristijonas Genevičius, Gytis Juška, and Ifor D.W. Samuel. Charge carrier mobility of the organic photovoltaic materials

PTB7 and PC71BM and its influence on device performance. *Organic Electronics*, 22(June):62–68, jul 2015.

[50] Jing Cui, Daniel E. Martínez-Tong, Alejandro Sanz, Tiberio A. Ezquerra, Esther Rebollar, and Aurora Nogales. Relaxation and Conductivity in P3HT/PC 71 BM Blends As Revealed by Dielectric Spectroscopy. *Macromolecules*, 49(7):2709–2717, apr 2016.

[51] Vishal Shrotriya, Jianyong Ouyang, Ricky J. Tseng, Gang Li, and Yang Yang. Absorption spectra modification in poly(3-hexylthiophene):methanofullerene blend thin films. *Chemical Physics Letters*, 411(1-3):138–143, 2005.

[52] X. Gong, M. Tong, Y. Xia, W. Cai, J. S. Moon, Y. Cao, G. Yu, C.-L. Shieh, B. Nilsson, and A. J. Heeger. High-Detectivity Polymer Photodetectors with Spectral Response from 300 nm to 1450 nm. *Science*, 325(5948):1665–1667, sep 2009.

[53] Hoyeong Kwon, Hamidreza Chalabi, and Andrea Alù. Broadband absorption with gradient metasurfaces. *EPJ Applied Metamaterials*, 5:4, 2018.

[54] Chen Guan Lee and Ananth Dodabalapur. Solution-processed high-k dielectric, ZrO 2, and integration in thin-film transistors. *Journal of Electronic Materials*, 41(5):895–898, 2012.

[55] Kun Xu, Shuxue Zhou, and Limin Wu. Dispersion of γ-methacryloxypropyltrimethoxysilane-functionalized zirconia nanoparticles in UV-curable formulations and properties of their cured coatings. *Progress in Organic Coatings*, 67(3):302–310, 2010.

[56] M. Notomi, H. Suzuki, T. Tamamura, and K. Edagawa. Lasing action due to the two-dimensional quasiperiodicity of Photonic quasicrystals with a penrose lattice. *Physical Review Letters*, 92(12):2–5, 2004.

[57] David Austin. Penrose tilings tied up in ribbons. *American Mathematical Society*.

[58] Branko Grunbaum and G.C. Shepard. *Tilings and Patterns*. New York : W.H. Freeman, 1987.

[59] J. Chan, A. D. Rakić, C. Y. Kwong, Z. T. Liu, A. B. Djurišić, M. L. Majewski, W. K. Chan, and P. C. Chui. Device optimization of tris-aluminum (Alq3) based bilayer organic light emitting diode structures. *Smart Materials and Structures*, 15(1), 2006.

[60] P. Dalasinski, Z. Lukasiak, M. Rebarz, M. Wojdyla, Artur Bratkowski, and Waclaw Bala. Photoluminescence , optical transmission and reflection of Alq 3 layers obtained by thermal evaporation deposition. *Opto-Electronics Review*, 12(4):429–434, 2004.

[61] Matthew D. Arnold and Martin G. Blaber. Optical performance and metallic absorption in nanoplasmonic systems. *Optics Express*, 17(5):3835, 2009.

[62] M. G. Blaber, M. D. Arnold, and M. J. Ford. A review of the optical properties of alloys and intermetallics for plasmonics. *Journal of Physics Condensed Matter*, 22(14), 2010.

[63] P. G. Etchegoin, E. C. Le Ru, and M. Meyer. An analytic model for the optical properties of gold. *Journal of Chemical Physics*, 125(16), 2006.

[64] Elison Matioli, Stuart Brinkley, Kathryn M. Kelchner, Yan-Ling Hu, Shuji Nakamura, Steven DenBaars, James Speck, and Claude Weisbuch. High-brightness polarized light-emitting diodes. *Light: Science & Applications*, 1(8):e22–e22, aug 2012.

[65] D. A. Japuntich. Polarized task lighting to reduce reflective glare in open-plan office cubicles. *Applied Ergonomics*, 2001.

[66] R. Clear and R. G. Mistrick. Multilayer polarizers: A review of the claims. *Journal of the Illuminating Engineering Society*, 1996.

[67] Yiqiao Tang, Timothy A. Cook, and Adam E. Cohen. Limits on fluorescence detected circular dichroism of single helicene molecules. *Journal of Physical Chemistry A*, 2009.